

MultiWavelength Analysis of a Solar Flare on 2002 April 15

Linhui Sui^{1,2}, Gordon D. Holman², Stephen M. White³, Dale E. Gary⁴, Kiyoto Shibasaki⁵,

and

Jie Zhang⁶

ABSTRACT

A detailed analysis of a solar limb flare on April 15 2002 was carried out with observations in X-ray, EUV, and microwave. The major findings are the following: (1) A low-cutoff energy at ~ 30 keV in nonthermal electron distribution is required to fit X-ray spectra of the flare. With this low-cutoff energy, the total energy of the nonthermal electrons is comparable to the total thermal plasma energy. (2) Several blob-like sources along a line above the flare loop later in the flare were likely to be caused by the magnetic islands due to tearing mode instability, suggesting the existence of a large-scale current sheet. (3) The optically thin free-free emissions contributed to the microwave images at both 17 and 34 GHz, but were radiated from the thermal plasma with lower temperature and larger emission measure than the plasma producing thermal X-rays. (4) A cusp-like structure above the flare loop seems to appear in microwave 34 GHz images near the peak of the flare. (5) The spectra of the nonthermal electrons obtained from the microwave spectra are much harder than those obtained from the X-ray spectra, agreeing with the previous findings.

Subject headings: Sun: flares—Sun: X-rays

¹Department of Physics, Catholic University of America, 620 Michigan Ave., Washington, DC 20064.

²Laboratory for Astronomy and Solar Physics, Code 682, NASA Goddard Space Flight Center, Greenbelt, MD 20771.

³Department of Astronomy, University of Maryland, College Park, MD 20742.

⁴Physics Department, New Jersey Institute of Technology, Newark, NJ 07102.

⁵Nobeyama Radio Observatory, National Astronomical Observatory of Japan, Minamimaki, Nagano 384-1305, Japan.

⁶Center for Earth Observing and Space Research, School of Computational Science, George Mason University, Fairfax, VA 22030.

1. Introduction

The period from 14 to 21 April 2002 was a time of moderate to high solar activity, due mainly to the transit across the disk of three large active regions: 9901, 9906 and 9907 (Gallagher et al. 2002). The Ramaty High Energy Solar Spectroscopic Imager (RHESSI, Lin et al. 2002) observed three flares (M3.7, M1.2, and M2.5 of GOES class) in the same active region (AR9901) on 2002 April 14-15, 15 and 16, as the active region approached the northwest limb. All three flares occurred within $\sim 10''$ in latitude and $\sim 30''$ in longitude of one another after allowing for solar rotation. They have similar light curves and morphological appearance, so can be considered homologous (Sui, Holman & Dennis 2004).

RHESSI soft X-ray (SXR) images of the April 15 flare most show a flare loop with bright looptop. In the standard flare models (Carmichael 1964; Sturrock 1966; Hirayama 1974; Kopp & Pneuman 1976), the flare loops are believed to be formed at higher and higher altitude because of the continuous upward motion of the magnetic reconnection site. Therefore, we would expect a continuous outward expansion of the flare loops. However, in the April 15 flare, Sui & Holman (2003) found that before the loop started to move outward, the altitude of the looptop centroid decreased at $\sim 9 \text{ km s}^{-1}$ in the early impulsive phase of the flare. This downward motion lasted about 2 min.

Besides the flare loop, there was a coronal source above the loop (Sui & Holman 2003). It was initially connected with the loop at the looptop before the impulsive phase started. After the impulsive phase started, the coronal source appeared to detach from the loop and stayed stationary for about 2 minutes before moving outward at 300 km s^{-1} . Sui & Holman (2003) found that the higher energy loops are located higher in altitude than the lower energy loops, while the high energy part of the coronal source located lower in altitude than the low energy part, indicating that the temperature of the underlying loops increased towards higher altitude, and the temperature of the coronal source increased towards lower altitude. These temperature distributions strongly suggest that the energy release or magnetic reconnection occurred between the top of the flare loop and the coronal source. Therefore, Sui & Holman proposed this was evidence for the existence of a large-scale current sheet.

The RHESSI observations of the other two flares on April 14-15 and 16 share some common features with the flare on April 15 (Sui, Holman & Dennis 2004): (1) A separate coronal source up to $\sim 30''$ above the flare loop appeared in the early impulsive phase and stayed stationary for several minutes. (2) Before the flare loop moved upward, the flare looptop centroid moved downward for 2-4 minutes during the early impulsive phase of the flare, falling by 13-30% of its initial height with a speed between 8 and 23 km s^{-1} , with the altitude in the 12-25 keV band decreasing more (except for the April 15 flare) and faster than that in the 6-12 keV band. (3) The downward motion of the looptop centroid occurred

over the same time range that the coronal source remained stationary. These new features were believed to related the formation or the development of the current sheet formation (Sui, Holman & Dennis 2004).

In this paper, we select the April 15 flare for a more detailed analysis because it was well observed with several other instruments at different wavelengths, such as: Nobeyama Radioheliograph (NoRH) and Owens Valley Solar Array (OVSA), Transition Region and Corona Explore (TRACE; 1600 Å). The associated coronal mass ejection (CME) was observed with SOHO/Large Angle and Spectrometric Coronagraph (LASCO).

2. Observations and Data Analysis

RHESSI observations of this event and their comparison with TRACE observations will be presented in section 2.1. The determination of the low-cutoff energy in the nonthermal electron distribution and the estimation of total energy in nonthermal electrons is studied in section 2.2. Microwave images and spectra are studied and then compared with the observations of the RHESSI observations in section 2.3.

2.1. RHESSI and TRACE observations

2.1.1. *RHESSI images*

RHESSI X-ray light curves in two energy bands (6-12, 25-50 keV) are shown in Fig. 1. The flare had a typical gradual rise and fall in soft X-rays (SXR). The impulsive phase had multiple peaks, with the major peak at 23:11:26 UT. The hard X-ray (HXR) flux (> 25 keV) increased abruptly at 23:09:40 UT, then decayed slowly after the impulsive phase. After 23:20 UT, RHESSI was in transit of South Atlantic Anomaly (SAA) and Earth eclipse (night time).

A consequence of RHESSI 10-20 keV are shown in Fig. 2. The images are dominated by the emission from a flare loop with its northern leg longer than the southern one, indicating nonsymmetrical loop morphology. Besides the flare loop, there is a coronal source above the loop, which appeared to be connected with the looptop in the rise phase of the flare. It suddenly separated from the underlying loop at the start of the impulsive phase on 23:09:40 UT, then stayed stationary for about 2 min before moving outward at 300 km s^{-1} (Sui & Holman 2003).

There was a CME associated with this flare. As indicated by SOHO/LASCO C2 and

C3 images (Fig. 3), a large coronal loop was seen propagating outward up to $16 R_{\odot}$ at an almost constant speed of $\sim 300 \text{ km s}^{-1}$. Sui & Holman (2003) estimated the location of the moving coronal source at 02:26:00 UT on 2002 April 16 when the large coronal loop was first seen in the LASCO C2 image, and found that at that time the RHESSI coronal source would have reached the inner edge of the coronal loop.

RHESSI images of different energy bands at the peak are shown in Fig. 4. At lower energies ($< 20 \text{ keV}$), the images show the flare loop with a bright looptop. At higher energies (20-50 keV), the images show two footpoints and a bright looptop source. The footpoints and HXR looptop source can be seen during the entire impulsive phase. Unlike the previously reported HXR looptop source (Masuda et al. 1994, 1995; Petrosian, Donaghy, & McTiernan 2002; Sui et al. 2002), the looptop source of this flare was always brighter than the two footpoints except at the major peak when the southern footpoint (indicated as ‘SF’ in the Fig. 4) was the brightest. Moreover, the southern footpoint was always brighter than the northern footpoint (‘NF’). An extra footpoint mentioned by Sui & Holman (2003) was carefully checked and approved not to be real footpoint, but part of the northern flare loop. Therefore, the RHESSI images seem to indicate that a simple flare loop system was involved in the flare.

One possible reason why the southern footpoint was brighter than the northern one is that the magnetic field intensity around the northern footpoint is stronger, leading to a stronger magnetic mirroring at the northern footpoint. Therefore, energetic electron beams dumped into the northern footpoint were weaker than the southern footpoint, causing weaker thick-target bremsstrahlung at the northern footpoint. This explanation is supported by the magnetogram obtained with the SOHO/Michelson Doppler Imager (MDI) shown in Fig. 5. The maximum magnetic field strength near the northern and southern footpoints are about -380 Gauss and +280 Gauss, respectively.

2.1.2. *RHESSI imaging spectroscopy*

The X-ray spectra of the two footpoints and looptop source at the major peak are plotted in Fig. 6. The flux of each source at each energy band was obtained by integrating the fluxes of pixels surrounding that source. Since only the RHESSI images above 20 keV clearly show the emission from the footpoints, the spectra of the two footpoints were only fitted to power-law spectra at the energy range between 20 and 50 keV. The power-law indices of the southern and northern footpoints are -4.5 and -3.8, respectively. Because the looptop source can be seen in images at energies from 6 to 50 keV, the looptop spectrum was fitted with a model consist of an exponential component due to thermal bremsstrahlung

(from 10 to 20 keV) and a power-law component (from 20 to 50 keV). The power-law fitting range was selected to be consistent with the energy range used for fitting the two footpoints. The emission measure and temperature of the thermal plasma are $2 \times 10^{46} \text{ cm}^{-3}$ and 30 MK, respectively. The power-law index of the looptop spectrum is -5.6, which is steeper than those of two footpoints, agreeing with the previous results (Masuda et al. 1994, 1995; Petrosian, Donaghy, & McTiernan 2002; Sui et al. 2002).

Unlike flares with symmetric loop morphology, such as the February 20, 2002 flare studied by Krucker & Lin (2002) and Sui et al. (2002), in which spectral slopes of the two footpoints were about equal, the spectrum of the northern footpoint in this event is harder by 0.7 than that of the southern footpoint. Assuming the energetic electrons were injected into the loops at the looptop region, we postulate two possible explanations for such different footpoint spectra: (1) more low-energy electrons were lost in Coulomb collision with ambient plasma when the injected electrons traveled through the longer (or northern) part of the loop (consequently called transportation effect); (2) non-uniform pitch-angle energy distribution of the accelerated electrons (specifically, the electrons with large pitch-angles are more abundant at low energies, and the electrons with small pitch-angle are more abundant at high energies) causes the more low-energy electrons (with softer spectrum) being mirrored back from the northern footpoint and dumped into the southern footpoint (consequently called acceleration effect). Of course, some combination of these two mechanisms could also be operating. Analysis of more events should be helpful in finding the most promising mechanisms.

2.1.3. TRACE 1600 observations

TRACE 1600 Å channel is sensitive to the plasma at the temperature range between 4.0 and 10×10^3 K (Handy et al. 1999), which is much lower than the plasma temperature sensitive to RHESSI (usually above 10 MK). Therefore, emissions in TRACE 1600 Å images mainly come from the transition region or lower chromosphere where usually footpoints or ribbons are located. TRACE 195 Å channel, which is sensitive to higher temperature ($5.0\text{-}20 \times 10^5$ K, and $1.1\text{-}2.6 \times 10^7$ K) plasma, did not observe the Sun that day.

In the rise phase of the flare (before 23:09:40 UT), TRACE Å images show two ribbons (left panel of Fig. 7). The two ribbons are somewhat parallel, but shifted. The one located at the north is about 30'' long, with the northeast end brighter than the rest of the ribbon; another one located at the south is about 20'' long, but brighter than the northern ribbon. The overlaid RHESSI 10-20 keV image clearly indicates that the flare loop connects the two ribbons.

When the impulsive phase started, a bright kernel suddenly appeared in the middle of the northern ribbon (right panel of Fig. 7). The brightness of the kernel varied during the impulsive phase. The higher flux spikes at RHESSI 25-50 keV corresponded to brightening of the kernel. The southern ribbon intensity also increased at those HXR spikes. During the impulsive phase when the location of the bright kernel of the northern ribbon can be determined, we do not find the location of the kernel changed. This means that not only the kernel did not move along the ribbon, but also the ribbon did not move obviously. As indicated by the right panel of Fig. 7, the northern footpoint in RHESSI images apparently corresponds to the bright kernel in the northern ribbon. The big, bright kernel in the southern ribbon corresponds to the southern, brighter footpoint. Therefore, TRACE images show a consistent nonsymmetrical flare morphology with RHESSI images.

In the decay phase, the distinct kernels along ribbons gradually disappeared, and therefore the ribbons became more uniformly bright, with the southern ribbon brighter than the northern one.

2.1.4. *Tearing mode instability*

As we introduced in section 1, in this April 15 flare, Sui & Holman (2003) proposed that there existed a large-scale current sheet between the coronal source above the flare loop and the HXR looptop source. Since the coronal source moved outward ($\sim 300 \text{ km s}^{-1}$) much faster than the rise of the looptop source ($\sim 10 \text{ km s}^{-1}$), the length of the current sheet will continuously increase. This elongation of the current sheet has been predicated by various flare model (e.g., Lin & Forbes 2000; Lin 2002). Because the current sheet cannot be rapidly dissipated by magnetic reconnection, it can exist for a few hours or even a few days, and extend many solar radii into the outer corona. There is some observational evidence for such current sheets associated with CMEs (Ciaravella et al. 2002; Ko et al. 2003; Webb et al. 2003).

Furth, Killeen, & Rosenbluth (1963) showed that a current sheet can be unstable to a process that significantly increases the rate of magnetic reconnection, the tearing mode instability. The tearing mode will change the magnetic topology along the current sheet, or, more specifically, the oppositely directed magnetic field lines along the current sheet will form blob-like magnetic island structures. Signatures of the tearing mode have been seen in Tokomaks, and we believe that, for the first time, we have detected such signatures in the RHESSI X-ray images of this flare.

In Fig. 2, a coronal source was seen separating from the underlying flare loop when

impulsive phase started. After staying stationary for about 2 min, the coronal source moved outward at $\sim 300 \text{ km s}^{-1}$. The coronal source was expected to exit the RHESSI image field of view around 23:13 UT. However, the many RHESSI 10-20 keV images between 23:13 UT and 23:18 UT still show several faint blob-like sources above the flare loop. Although the location of these sources changed from time to time, they seemed to be always located along the same line, which is along the presumed current sheet. Two of such images are plotted in Fig. 8. Therefore, we believe these blob-like sources may be the magnetic islands produced by the tearing mode instability.

It is possible that these blobs could be artifacts of the RHESSI image processing. But the appearance of these blobs in the expected location, at different times, in different energy bands in the RHESSI images constructed with different imaging algorithms, argues against this possibility. The ongoing efforts by RHESSI team in improving the RHESSI image dynamic range should be helpful to further check the reality of these sources.

2.2. Low-cutoff energy in the nonthermal electrons

2.2.1. Review of studies on the low-cutoff energy

Most of flare X-ray spectra have a negative power-law (single or double power-law) component at their high energy range (Dennis 1985; Lin et al. 1987; Dennis 1988; Winglee et al. 1991). Although a thermal bremsstrahlung models with multiple temperature plasma may also be able to fit the data (Brown 1974; Emslie & Brown 1980; Brown & Emslie 1987), this power-law spectra are generally believed to be produced by the nonthermal bremsstrahlung emission from the electrons with a power-law distribution. In order to ensure the total nonthermal electron number to be finite, mathematically we have to introduce a low-cutoff energy for the nonthermal electron distribution. So far, the physics of the low-cutoff energy is still unclear.

Determination of the low-cutoff energy in the electron distribution is critical in estimating the total energy of the nonthermal electrons, therefore providing an important constraint on acceleration mechanisms in flares (Miller et al. 1997). The previous estimations of the total electron energy have been often made with assumed (arbitrary) cutoff energies at the range of 20-30 keV (Dennis et al. 2003, and reference therein). The total energy of the injected energetic electrons is very sensitive to the low-cutoff energy, in particular, in the flares with steep (or soft) spectra. For instance, if the electron has a distribution $\sim E^{-\delta}$, where δ is typically in the range of 3~8 (Dennis (1985), say δ is 6, assuming thick-target interactions, then the total electron energy with a cutoff at 10 keV is almost two order of

magnitude larger than that with the cutoff at 30 keV. Because of the uncertainties like this, Hudson (1986) claimed that not a single component of the flare energy budget was known to better than an order of magnitude.

Flare spectra flatten at the photon energies below the low-cutoff energy in the electron distribution. However, either because of high minimum photon energy detectable by the hard X-ray spectrometers (typically 20 keV), or because of the presence of thermal bremsstrahlung at low energies, the low-cutoff energy in the electron distribution has been difficult to identify. Holman & Benka (1992) claimed that the low-cutoff energy may in fact be determined by the spectral transition from thermal to nonthermal bremsstrahlung. Low-cutoff energies ranging from 20-40 keV were obtained with this hybrid thermal/nonthermal model (Benka & Holman 1994). Gan (2001) and Gan et al. (2002) have found that many of the broken (or double) power law spectra obtained from BATSE on the Compton Gamma Ray Observatory (CGRO) were consistent with the flattening that results from a low-cutoff energy ranging from 45-97 keV. A low-cutoff energy as high as 73 keV has also been used to fit RHESSI spectra for the 2003 July 23 γ -ray line flare (Holman et al. 2003).

All the studies we discussed above have only demonstrated the electron bremsstrahlung model with a certain low-cutoff energy could fit a power-law spectrum. However, the low-cutoff energy being used is not uniquely determined. Other energies may be able to fit the same spectrum as well. There have been some ways being proposed to give a better estimate of cutoff energies. For instance, Holman (2003) pointed out that after knowing the effects of low-cutoff energy on both microwave and hard X-ray spectra of a same flare, we may be able to find a cutoff energy consistent with both data sets.

RHESSI X-ray spectra at the peak of flares typically show two components: an exponential (presumably thermal) component at low energies (≤ 30 keV) and a flatter power-law (presumably nonthermal) component at higher energies. The two components merge smoothly together. Because the RHESSI spectra extends down to 3 keV (when both RHESSI attenuators are out of the field of view), one obvious improvement in determining the low-cutoff energy is that we can not arbitrarily set the cutoff as previously done. Instead, we are able to identify upper limits of the low-cutoff energies for flares whose spectra clearly consist of an exponential component and a power-law component, such as the 2003 July 23 γ -ray line flare studied by Holman et al. (2003). Any energy below that limit can still be used to fit data because at low energies (e.g., <10 keV), the fluxes contributed from the nonthermal bremsstrahlung are usually much less than those from the thermal bremsstrahlung, so the spectra flattening due to the low-cutoff energy has no effect on the total spectra. However, the spectra of the April 15 flare show a distinctive feature, so the low-cutoff energy can be almost uniquely determined.

Since the thin attenuators of the RHESSI spectrometer were in during the flare period, the effective area of the detectors drops rapidly as the photon energy falls below 10 keV (Smith et al. 2002). The current uncertainty in the correction factor is large at these energies, so fluxes below 10 keV were not included for spectral fitting in this paper.

2.2.2. Derivation of the Low Energy Cutoff

Before the impulsive rise at 23:09:40 UT, the RHESSI spatially integrated spectra are well fitted with a model solely consist of an isothermal bremsstrahlung spectrum (exponential form) within a range between 10 and 20 keV. The *upper left panel* of the *Fig. 9* shows one of such spectra. The temperature of the thermal plasma is about 30 MK, with the emission measure of $2.0 \times 10^{47} \text{ cm}^{-3}$.

When the impulsive phase started, most of the flare spectra (such as the one shown in the *upper right panel* of the *Fig. 9*) obviously have a power-law component above 20 keV. However, because of its steep power-law spectra, if allowing a very low cutoff energy (say 10 keV), the fluxes contributed from the nonthermal, power-law component at low energies would be higher than those from the thermal, exponential component. Based on the RHESSI lightcurves (upper panel in Fig. 1), such scenario cannot be true because the thermal emission always dominated at low energies.

To fit the spectra at the impulsive phase, we use a model consist of a thermal bremsstrahlung component and nonthermal thick-target bremsstrahlung component with a constant low-cutoff energy. The determination of the low-cutoff energy has to ensure (A) the nonthermal power-law spectra will not dominated over thermal spectra at low energies; (B) the thermal parameters, i.e. temperature and emission measure, have a smooth and gradual increase over the transition from the rise to the impulsive phase of the flare. After several trials, a low-cutoff energy of 30 keV in electron distribution was found to meet these two requirements. Moreover, with this low-cutoff energy, the model also nicely fit the spectrum at the peak of the flare (*bottom panel* of the *Fig. 9*), which clearly shows an exponential component (thermal component) at energies above 10 keV. When no HXR 25-50 keV fluxes were produced later in the flare (after 23:16 UT), the spectra were fitted with a model only consist of a thermal bremsstrahlung component.

The time profiles of the fitting parameters are plotted in Fig. 10. As expected, both the time profiles of plasma temperature (*panel b*) and emission measure (*panel c*) are smooth throughout the flare. For comparison purpose, the GOES temperature and emission measure, determined using the program GOES_TEM.PRO in the Solar Software Tree, which was

developed from the concepts of Garcia (1994) and Thomas et al. (1985), are also plotted in the same figure. The temperatures from GOES are consistently lower than those from RHESSI, while the emission measures from GOES are always larger than those from RHESSI. The plot of the photon spectral index (*panel d*) shows a typical soft-hard-soft pattern (e.g., Dennis 1985).

Although the 30 keV low-cutoff energy was obtained by fitting the spectra, surprisingly, the fitting results are also supported by the RHESSI images. In the fitted spectra shown in the *upper right and bottom panel* of the *Fig. 9*, the thermal bremsstrahlung dominates the spectra below 20 keV, while the nonthermal bremsstrahlung dominates the spectra above 20 keV. Interestingly, RHESSI images (*Fig. 4*) below 20 keV all show the flare loop, suggesting dominated thermal emission. The images above 20 keV most show the two footpoints and hard X-ray looptop source, implying dominated nonthermal emission. This consistency between the fitted spectral and the RHESSI images makes the 30 keV low-cutoff energy more reliable.

2.2.3. Total Energy of the nonthermal electrons

1. Review of previous studies on total nonthermal energies

It has been of interest for decades to compare the total energy of nonthermal electrons with the thermal energy of the hot plasma. Such studies can tell us whether flares convert most of their energy directly to heat the plasma or they spend a large portion of energy to accelerate the particles, which has been one of the key issues to understand the flaring process. As pointed out by Dennis et al. (2003), for the most of 30 flares observed with the Hard X-Ray Burst Spectrometer (HXRBS) of the Solar Maximum Mission (SMM), the total energy in the accelerated electrons (>25 keV) was much larger than the energy in thermal plasma.

However, two uncertainties in the measurements compromised the study of the energy budge. Firstly, as we motioned above, incapability in obtaining the low-cutoff energy in non-thermal electron distribution severely affect the estimation of the total energy in electrons. The 25 keV reference energy in the study of SMM flares was set to be equal to the lower energy threshold of the scintillation HXRBS (Dennis et al. 2003). If allowing 10 keV cutoff, the total nonthermal energy in those SMM flares will be an order of magnitude larger. On the contrary, if the cutoff energy is much higher, as claimed by Gan (2001) and Gan et al. (2002), the energy in the nonthermal electrons will be less than the energy in thermal plasma. In the 2003 July 23 γ -ray line flare, Holman et al. (2003) got the highest low-cutoff energy by fitting the RHESSI spectra, therefore obtained the minimum total energy in the nonthermal

electrons. They found the minimum total energy of nonthermal electrons is on the order of the energy in the thermal plasma. Secondly, the uncertainty of filling factor. The thermal energy could be less if the filling factor is less than one (the thermal energy proportional to the square-root of the filling factor). So far, no improvement in determination of the filling factor has been made.

2. Calculation of the total energy in the nonthermal electrons

Since we have demonstrated that the low-cutoff energy we obtained in the April 15 flare was not arbitrarily selected, instead, it was determined by spectral fitting. Therefore, we believe it will provide more accurate estimation of the total energy in nonthermal electrons.

The total thermal energy is calculated using:

$$E = \sqrt{EM \cdot V \cdot Q} \cdot 3 \cdot K \cdot T \quad (1)$$

where V is the volume of the thermal plasma, EM and T are emission measure and temperature, Q is the filling factor (set to 1). EM and T from GOES and RHESSI have been obtained in section 2.2.2. Because GOES does not have soft X-ray image, the GOES source volume is set to be equal to that of RHESSI. The accumulated nonthermal energies of electrons are the summation of nonthermal electron energy of each time interval up to the time of interest.

The thermal energy in the hot plasma obtained from both GOES and RHESSI, and the total accumulated energy of the nonthermal electrons with energies above the low-cutoff energy (i.e. 30 keV) are plotted in the bottom panel of the Fig. 10. The thermal energy obtained from GOES is ~ 2 times higher than the thermal energy obtained from RHESSI. It is obvious that the accumulated nonthermal electron energy ($\sim 6 \times 10^{29}$ ergs) is almost equal to the maximum thermal energy obtained from GOES, agreeing with the recent results made by Holman et al. (2003) and Emslie et al. (2004).

2.3. Microwave images and spectra

2.3.1. Review of microwave flare observations

Because both microwave and hard X-ray emissions are produced by highly energetic electrons with different emission mechanism, the observations at two wavelength regimes offer us information on different aspects of conditions in the solar atmosphere where flares occur White et al. (2003). Bremsstrahlung is produced by collisions, and therefore requires

high densities. Gyrosynchrotron microwave radiation is extremely efficient and allow us to detect electrons at energies of hundreds of KeV even when their densities are very low.

Previous studies have shown that the time profiles of flares at both X-ray and microwave wavelengths are very similar (Silva, Wang, & Gary 2002, and reference therein), indicating a common origin of electrons. After analyzing both microwave and hard X-ray spectra in 27 solar flares, Silva, Wang, & Gary (2002) found 65% of 27 flares they analyzed indicated a delay larger than 2 s. They also found that about 75% the flares they studies, the inferred power-law index of the electron energy distribution from the microwave electron is harder than that from the X-ray spectra by average 2.0 ± 0.7 for nonimpulsive phase (the individual microwave peaks at the impulsive phase display a slow rise and decay with a total duration of more than 2 min) and 0.8 ± 1.0 for impulsive flare. As summarized by Silva, Wang, & Gary (2002), the difference in the indices of the electron energy spectrum may be explained (1) by two different electron populations being accelerated in different sites with distinct physical conditions, (2) by a second-step acceleration mechanism, (3) by a “trap-plus-precipitation” model.

The previous study of comparing radio and HXR images (Nishio et al. 1997, and reference therein) suggested that two flare loops with different size were often involved in flares. The microwave emission comes from both loops, while hard X-ray emission is preferentially from the smaller loop.

Most of previous comparisons of HXR images and radio images involve HXRs below 50 keV whose source is dominated by electrons with energies much lower than those that typically produce the nonthermal microwave emission. Recently, White et al. (2003) present the first comparison between radio images of high-energy electrons and images of hard X-rays produced by the same electrons at photon energies above 100 keV. They found that the power-law indices (i.e., 1.8-2.6) of high-energy electron obtained from radio spectra were still much smaller than those obtained from RHESSI X-ray spectra (i.e., 4.5-5.).

This April 15 flare was observed by Nobeyama Radioheliograph (NoRH), Nobeyama Radio Polarimeters (NoRP) and Owens Valley Solar Array (OVSA). NoRH consists of 84 parabolic antennas with 80 cm diameter. The observing frequencies are 17 GHz and 34 GHz with spatial resolutions of 10 arcsec and 5 arcsec, respectively. The temporal resolution is 1 s, and the field of view is full solar disk. Nobeyama Radio Polarimeters (NoRP) are observing the Sun at multiple frequencies (1, 2, 3.75, 9.4, 17, 35, and 80 GHz) with temporal resolution of 0.1 s. It is capable to obtain the total microwave flux from the Sun.

Owens Valley Solar Array (OVSA) is a solar-dedicated, frequency-agile interferometer, which currently consists of two 27 m antennas and four 2 m antennas. The four 2 m antennas

view the whole solar disk, and the two 27 m antennas only look at a part of the Sun. Its receiver can be tuned to harmonics of 200 MHz in the range of 1.0-18.0 GHz. For the event studied in this paper, OVSA was observing at 38 frequencies. The time cadence is 4s for the total power.

NORH provides excellent microwave images for this event. However, the microwave fluxes above 10 GHz from NORP were affected by the cloud during the observation, therefore, we could not obtain reliable microwave spectra from NORP. Instead, the microwave spectra were obtained with OVSA. Since one of OVSA's two 27 m antennas did not observe the flare region, we could not reconstruct microwave images using OVSA. Therefore, the microwave data from NORH and OVSA supplement each other for this event.

2.3.2. *NORH observations*

The time profiles of the microwave fluxes at 17 GHz and 34 GHz are shown in the *lower panel* of Fig. 1. The 17 GHz fluxes increased slowly as early as 23:00 UT, almost 10 min before the impulsive phase started. It is striking that right before the impulsive rise (23:07-23:09:40 UT), even very small flux increase in RHESSI 25-50 keV corresponded to the 17 GHz flux increase at the same time. Evidently, the spikes at 17 GHz during the impulsive phase correlate very well with the spikes in RHESSI 25-50 keV band, suggesting dominated nonthermal radiations at 17 GHz. During the decay phase (i.e. after 23:16 UT) when X-rays fluxes below 25 keV was decreasing, the 17 GHz maintained a flux level 4 times above the background and increased slowly until 23:23 UT. This time profile difference during the decay phase suggested that 17 GHz fluxes were free-free emissions radiated from thermal plasma which has different temperature and emission measure from X-rays emitting thermal plasma.

Unlike 17 GHz, the fluxes at 34 GHz did not increase until the impulsive phase started. After the that, the 34 GHz fluxes increased gradually and steadily during most of the flare, except a short spike around 23:11:30 UT, which corresponded to the major peak in both 17 GHz and HXR at 25-50 keV. The fluxes of 17 and 34 GHz after 23:16 UT were about equal, indicating a flat spectrum due to thermal emission. Like 17 GHz, the gradual increase of 34 GHz fluxes also had peak around 23:23 UT. Notice that the time profile of 34 GHz is roughly similar to that of soft X-ray fluxes (1-8 Å) from GOES (except in the rise phase and at the major peak).

The NORH microwave maps at 17 and 34 GHz shown in *Fig. 11* are mostly different. Throughout the flare, the images at both frequencies reveals very interesting evolution of

different microwave radiation mechanisms. Starting at 23:00 UT, the 17 GHz images seem to show some emission from the active region and coronal sources above it. They look very different from the later images when the flare fully developed. After 23:05 UT, the 17 GHz images started to show two ends of a flare loop, with the northern end much brighter than the southern one (panel A in Fig. 11), suggesting the nonthermal gyrosynchrotron emission. As pointed out in section 2.1, the magnetic field near the northern footpoint was stronger. Therefore, the gyrosynchrotron emission should be stronger near that footpoint. When the impulsive phase started at 23:09:40 UT, the images (panel B, D, D in Fig. 11) were still dominated by footpoint emissions, with the northern footpoint still much brighter than the southern one. Meanwhile, the 17 GHz images seem to show some weak emissions from the loop, which were likely due to the free-free emissions. The images between 23:16 and 23:26 UT (panel E in Fig. 11) most showed the two footpoints with comparable brightness and some emission from the loop, suggesting a completely different radiation mechanism: optically thin free-free emission. This interpretation is in agreement with the gradual time profile after 23:16 UT. All the images after 23:26 UT (panel F in Fig. 11) only showed a flare loop with the southern half of the loop brighter than the northern half.

The 34 GHz images do not show any identifiable source until the start of the impulsive phase at 23:09:40 UT, which is consistent with the time profile during that period. Between 23:09:40 and 23:11:20 UT, all the 34 GHz images show the flare loop. The two ends of the flare loop, with comparable brightness, were brighter than the rest of the loop. These images suggest thermal free-free emission, in agreement with the gradual flux increase in time profile during that period. The two bright loop ends, which are similar to the 34 GHz images between 23:16 and 23:26 UT when free-free emission dominated, indicate that the density of the plasma contributing to the microwave emission is higher at the footpoint. The images between 23:11:20 and 23:11:50 UT, when the time profile of 34 GHz had a spike, were dominated by the emission near two ends of the loop, with the northern end brighter than the southern one, suggesting dominated nonthermal gyrosynchrotron. All the images after 23:11:50 UT show the flare loop, with its southern half brighter than the northern half, similar to the 17 images after 23:26 UT.

2.3.3. *Cusp structure in microwave images*

Besides the flare loop and footpoints, the NORH microwave images during the impulsive phase at both 17 and 34 GHz show a cusp-like structure above the loop, like those observed with Yokoh/SXT (Tsuneta et al. 1992). The cusp can be seen in 34 GHz image at 23:11:20 UT (bottom-left panel in Fig. 11, indicated by an arrow) and 17 GHz image

(Fig. 12) around the peak of the flare (23:11-23:12:30 UT).

Further analysis indicates that the cusp-like structure at 17 GHz during the peak might just be free-free emission from the coronal source above the active region which existed before the flare started. As we mentioned earlier, in the early rise phase between 23:00-23:05 UT, the 17 GHz images showed some emissions of the active region and coronal sources above it. To check whether those coronal sources contribute to the cusp at the peak, we subtract the average of the 17 GHz images during 23:00-23:05 UT from the peak images apparently showing the cusp in Fig. 12, and find that the cusp disappears in all the subtracted images, suggesting that the cusp structure existed even before the flare started. Therefore, the cusp at 17 GHz might just be active region free-free emission underneath the flare loop that looked like the cusp due to projection effects.

Similarly, we subtract the average of the 34 GHz images during 23:00-23:05 UT from the 34 GHz image at the 23:11:20 UT, and find that the cusp remains in the image. This is not surprising because during the rise phase, the 34 GHz images do not show any identifiable source. Therefore, the subtracted images will not be much different from the original images. This seems to suggest that the cusp in 34 GHz images might be a real cusp. As we mentioned earlier, the 34 images at the peak were dominated by nonthermal gyrosynchrotron emission, but based on its time profile at the peak, there must be some contributions from thermal emission too. Since there is only one image unambiguously showing the cusp, it is difficult for us to judge whether it is due to thermal or nonthermal emission.

2.3.4. Comparison of Microwave images with X-ray images

As we have discussed above, although NORH 17 GHz and RHESSI 25-50 keV images can show emissions from the nonthermal electrons, the 17 GHz images are more capable in detecting these electrons. This can be demonstrated in the rise phase of the flare when the electron beams were not strong. As indicated by the RHESSI light curve (*Fig. 1*), there were some weak HXR fluxes in the 25-50 keV band about 2 min before the start of the impulsive phase. However, RHESSI 25-50 keV images could not show any identifiable source until the impulsive phase started. While as early as 23:05 UT, almost 5 min before the impulsive phase started, the 17 GHz images clearly show two ends of the flare loop. Such difference between X-ray and microwave images supports the theory that the gyrosynchrotron is a more efficient than the bremsstrahlung. More importantly, the microwave observations also indicate that nonthermal electron beams were indeed produced even before the impulsive phase started. But whether such weak electron beams can account for the plasma heating during the rise phase, as indicated by the steady increase of the 6-12 keV fluxes during the

period (upper panel of *Fig. 1*), is unclear.

Although RHESSI 10-20 keV images, the 17 GHz images at the decay phase, and most of the 34 GHz images all show thermal bremsstrahlung in the flare, the microwave at both frequencies seems to be produced from the plasma with lower temperature than X-ray-emitting plasma. The 10-20 keV images always show a flare loop with a brighter looptop (*Fig. 13*), while the 17 and 34 GHz images showed either brighter footpoint or southern half of the loop. In the standard flare model, the magnetic reconnection is believed to occur above the loop, so the looptop region should be hotter than the rest of loop. This may also explain why the plasma blob (with temperature at ~ 30 MK) above the flare loop, seen in RHESSI 10-20 keV images (*Fig. 2*), did not appear in any of the NORH images.

In the next section, we quantitatively prove that the plasmas observed by GOES and RHESSI could not produce enough microwave emission to account for the microwave fluxes observed with the NORH.

2.3.5. Comparison of predicated and observed free-free microwave fluxes

Based on the time profile and images of 34 GHz, we have concluded that the thermal bremsstrahlung emission (or free-free emission) dominated during most of the flare. The difference between the RHESSI and NORH images further suggests that the plasma seen by RHESSI is hotter than that seen by NORH. In order to quantitatively test this argument, we calculate microwave emissions produced from the plasma observed by RHESSI and GOES, and then compare them with observed NORH fluxes at 34 GHz.

In section 2.2.2, We have derived the temperatures and emission measures of the thermal plasma observed with GOES and RHESSI (*Fig. 10*). Assuming free-free emission, we compute the microwave fluxes at 34 GHz using the formula:

$$f(\nu) = \frac{3 \cdot 10^{-20}}{AU^2 \sqrt{T}} EM (17.7 + \log \frac{T^{1.5}}{\nu}) \quad (2)$$

Where $f(\nu)$ is the microwave flux at frequency ν , AU is the distance between the Earth and the Sun, T and EM are the temperature and emission measures. The calculated 34 GHz fluxes are plotted in *Fig. 14*.

It is evident that the calculated fluxes from both GOES and RHESSI are less than the observed 34 GHz flux throughout the flare. The fast flux increase of the calculated fluxes from both GOES and RHESSI coincided in time with the fast increase of the observed flux, confirming the thermal origin of the microwave fluxes. After 23:13 UT, the fluxes from GOES

plasma are about half of the observed fluxes, whereas the fluxes from RHESSI plasma are about one order of magnitude less. This further suggests that thermal microwave fluxes at 34 GHz were produced by the plasma with lower temperature (therefore larger emission measure) than the plasma producing X-rays. Since the microwave free-free emission is more sensitive to change of the emission measure than to the temperature, we conclude that the plasma with twice the emission measure of GOES plasma will be able to produce the observed microwave flux at 34 GHz.

Since the equation (2) is not sensitive to the frequency ν , all the estimations we did at 17 GHz also applies to 34 GHz. Therefore, the observed fluxes at 17 GHz during the decay phase must also be produced by cooler plasma than the X-ray emitting plasma.

2.3.6. Comparison of the nonthermal microwave-emitting and X-ray emitting electrons distributions

As we mentioned earlier, the microwave-emitting electrons usually have a harder spectra than the X-ray-emitting electrons (e.g., Silva, Wang, & Gary 2002). In this section, we will make a similar comparison of power-law indices of the nonthermal electrons for this event.

The power-law indices of the X-ray emitting electrons are obtained directly from fitting the RHESSI spectra (see section 2.2.2). The power-law indices for the microwave-emitting electrons are obtained from fitting the optical thin part of the OVSA spectra. We selected two time intervals (intervals a, b in Fig. 15), i.e. 23:10:20-23:10:40 UT, 23:11:20-23:11:40 UT, which are near two spikes in both HXR and Microwave fluxes (see top panel of Fig. 15). The X-ray spectra at these two time intervals are plotted in the middle two panels of Fig. 15. The power-law indices of the X-ray emitting electron are -6.8 and -6.0 for the first (left panel) and second (right panel) intervals, respectively. The OVSA microwave spectra are plotted in the bottom panels in Fig. 15. Linear fits to the optically thin part (from 12 to 18 GHz) of the two spectra gave the slopes, α , of -1.35, and -1.08 for the first and second intervals, respectively. With the empirical formula from Dulk (1985):

$$\delta = 1.11\alpha + 1.36 \quad (3)$$

the power-law indices of the microwave-emitting electron, δ , would be -2.8 and -2.5. Therefore, the difference of electron power-law indices are 3.5-4.0, which is much larger than the 2.0 ± 0.7 found by Silva, Wang, & Gary (2002) for similar nonimpulsive events in their samples.

One possible explanation why we obtained such hard spectra for the microwave-emitting electrons is that the part of the OVSA spectra (from 12 to 18 GHz) we fitted might not be

fully optically thin. As indicated by the OVSA spectra, the peak (or turnover) frequency is around 9 GHz, and the transition from optically thick (below the peak frequency) to optically thin (above the peak frequency) region is not a sharp turnover, so we suspect the part of spectra we fitted are not totally optically thin. Another possibility is that contributions from the thermal free-free emissions will affect the results. Based on the time profile of the OVSA flux at 12.4 GHz (top panel in Fig. 15), during decay phase (after 23:16 UT) the microwave fluxes stay higher than the fluxes in the rise phase, similar to the light curves of NORH 17 and 34 GHz, which suggests the thermal contributions.

To correct the OVSA results, we estimate the power-law indices of nonthermal electrons using NORH data. By doing so, the concern of the broad turnover from optically thick to optically thin should not exist, because the 17 and 34 GHz are very higher than the turnover frequency. But the thermal free-free emissions still contribute at both frequencies, particularly, for the 34 GHz, so we have to subtract these thermal fluxes before we estimate the electron power-law indices.

For a rough estimate, the thermal fluxes at the impulsive phase are obtained from linear extrapolation of the fluxes in the rise and decay phases. The nonthermal fluxes (thick solid lines) around the major peak shown in *Fig. 16* are obtained by subtracting the thermal fluxes (dotted lines) from the total fluxes (thin solid lines) at both frequencies. We then obtain the slopes of the optically thin part of the spectra using the deduced nonthermal fluxes at 17 and 34 GHz. After applying to equation (3), we obtain the power-law indices for the microwave emitting electrons around the major peak at the impulsive phase (inset of *Fig. 16*). The power-law index at the peak is about -4.0, steeper by 1.5 than that obtained with OVSA at the same time. Compared with the power-law index of the X-ray emitting electrons at that same time (i.e., -6.0), the spectra of the microwave emitting electrons is still harder by 2.0. However, this difference is within the range obtained by Silva, Wang, & Gary (2002).

3. Summaries and discussions

3.1. Summaries of RHESSI and TRACE observations

We have analyzed the April 15, 2002 using the multi-wavelength observational data. The RHESSI images at 10-20 keV band showed a nonsymmetrical flare loop, with a coronal source located above the loop. The coronal source appeared to be attached to the loop in the rise phase of the flare, and then separated from the loop when the impulsive phase started. After the separation, the coronal source maintained stationary for about 2 min before moving outward at 300 km s^{-1} . The hotter part of the coronal source was found to be located lower in

altitude than the cooler part, suggesting the existence of a large-scale current sheet between the flare looptop and the coronal source where the magnetic reconnection occurs (Sui & Holman 2003) .

Later in the flare when the coronal source above the loop are believed to have exited the RHESSI image field of view, the RHESSI 10-20 keV images showed several faint, blob-like sources along the trajectory of the initial coronal source. Although the location of these sources changed from time to time, they were always located along this trajectory. We believe these blob-like sources may be magnetic islands initiated by the tearing mode instability. Such features further support the existence of the large-scale current sheet.

Before the flare loops apparently expand upward, the looptop centroid was found to maintain its altitude in the rise of the flare, and then move downward for about 3 min when the early impulsive phase started (Sui & Holman 2003; Sui, Holman & Dennis 2004). The downward motion of looptop centroid, which has been interpreted as altitude decrease of the loops, is likely due to formation or development of the current sheet in the early impulsive phase. When the loops expanded upward, the loops seem to grew toward the coronal source above the loop (Sui, Holman & Dennis 2004), which also support the existence of a current sheet above the loop.

There is a CME associated with the flare. The CME propagated outward at a constant speed of 300 km s^{-1} , the same speed as the outward motion of the coronal source above the loop observed with RHESSI. Although the coronal source could catch the CME front loop when the CME loop was first seen in LASCO C2 images, it does not mean the coronal source in RHESSI images is the same as the CME loop. It may just suggest that the coronal source and the CME loop were produced by a same mechanism.

The nonsymmetrical loop morphology is consistently revealed by RHESSI, TRACE 1600 Å, and NORH images. The RHESSI images at energies above 20 keV show a looptop source and two footpoints, with the southern footpoint brighter than the northern one. The two footpoints in RHESSI images coalign with bright kernels in two ribbons shown in TRACE 1600 Å images. The southern brighter, larger footpoint is consistent with brighter, larger kernel in the southern ribbon. The NORH microwave images show an opposite nonsymmetrical brightness for the two footpoints, with the northern footpoint much brighter than the southern one. This apparent contradiction can be reconciled if the magnetic field near the northern footpoint was stronger than the southern footpoint, leading to stronger gyrosynchrotron and electron mirroring near the northern footpoint, therefore weaker bremsstrahlung at the northern footpoint. Such nonsymmetrical magnetic field near two footpoints was indeed supported by the MDI magnetogram before the flare.

Usually the HXR looptop source is much weaker than the two footpoints (Masuda et al. 1994, 1995; Petrosian, Donaghy, & McTiernan 2002; Sui et al. 2002). However, the HXR looptop source in this flare was brighter than the two footpoints during most of the impulsive phase (except at the peak). This may be the reason why it was labeled as one of the two “discovery” events for RHESSI by Veronig & Brown (2004). They found that this bright HXR looptop source might be due to thick-target bremsstrahlung from electron beams collisionally stopped within the loop due to very high loop column densities (Veronig & Brown 2004; Veronig et al. 2004).

3.2. Lessons learned from the derivation of the low-cutoff energy

Before RHESSI was launched, the electron low-cutoff energy was either decided by the lower-energy limit of spectrometers or arbitrarily set to a convenient value (e.g., Dennis et al. 2003; Holman 2003), therefore, leading to a big uncertainty in estimating the total energy of the nonthermal energies in flares. In this event, the low-cutoff energy, for the first time, is required by RHESSI spectral data. Because of its steep power-law spectra, if we do not set a low-cutoff energy in nonthermal electrons, the fluxes of the power-law nonthermal component of the spectra would be stronger than the thermal component at lower energies during the impulsive phase. This is contradictory to the fact that thermal dominates at low energies (below 15 keV). In order to ensure the dominance of thermal flux at low energies and smooth increase of the thermal parameters over the transition from the rise to the impulsive phase of the flare, we found that the low-cutoff energy of nonthermal electrons have to be around 30 keV. The spectral fitting results with this low-cut off energy is surprisingly consistent with RHESSI images, because they both indicate that the energy range of transition from thermal dominance to nonthermal dominance is around 20 keV. With this 30 keV low-cutoff energy, we found that the total energy of nonthermal electron is about to equal to the total thermal energy, indicating that flares are good accelerators for electrons, in agreement with recent findings (e.g. Holman et al. 2003; Emslie et al. 2004). Although there are several acceleration mechanisms being proposed in the literatures (see review by Miller et al. 1997), It is still not clear how these electrons are accelerated exactly.

This event might be very special because of its steep power-law spectra. For most of the flares, the power-law component will not dominate over thermal component at lower energies even without setting a low-cutoff energy. Therefore, the method we used for this event to estimate the low-cutoff energy may not be applied universally. However, we did learn a couple of useful points from this analysis.

- (1) Instead of fitting only one or a few spectra, we should fit multiple spectra throughout

the flare to find the most reasonable models. As a matter of fact, some of the spectra during the impulsive phase of the flare can also be purely fitted to single power-law spectra all the way down to 6 keV. However, this kind of fitting scenario will be contradictory to the spectra in the rise phase which indicates that the spectra at lower energies are thermal. Sui et al. (2002) has pointed out that multiple models could be used to fit a same RHESSI spectra even with its highest up-to-date energy resolution. So the difficulty is to how to find the correct model. Certainly, by fitting multiple spectra throughout the flare to check for consistency will offer some help. We can also try to utilize other sources of information, such as checking the low-cutoff energy effect in microwave spectra as proposed by (Holman 2003), checking plasma temperature using iron lines in RHESSI spectra (Dennis & Philips, private communications).

(2) The spectral fitting results should be checked with the RHESSI images for consistency. For instance, we can check whether the energy ranges in the fitted spectra dominated by thermal/nonthermal are also dominated by thermal/nonthermal in images. Usually the flare loops are due to thermal bremsstrahlung emission, and footpoints are due to nonthermal bremsstrahlung emission. However, we have to be careful in judge which source is thermal and nonthermal in X-ray images. For instance, Holman et al. (2003) found that a single large coronal source in the rise phase of the July 23, 2002 X4.8 flare could not be fitted by an isothermal bremsstrahlung model. Instead, they could be fitted with a broken power-law model.

3.3. Summaries of microwave observations

The NORH images of this event indicate that microwave emissions are contributed from both nonthermal gyrosynchrotron and thermal free-free emission. At 17 GHz, the gyrosynchrotron dominated during the rise and impulsive phase of the flare, while free-free emission dominated during the decay phase. At 34 GHz, the free-free emission dominated most part of the flare, except at the peak when the gyrosynchrotron dominated. One interesting finding in both 17 and 34 GHz images is the appearance of the cusp-like structure above the flare loop around the peak of the flare. However, the cusp at 17 GHz is most likely due to free-free emission from an active region behind the flare loop, which existed before the flare started. It is unclear whether the cusp at 34 GHz is thermal or nonthermal because it only appeared in one image at the peak. If it is nonthermal, then it might be the first direct evidence showing the transportation of nonthermal electrons from above the flare loop.

Although thermal bremsstrahlung emissions contribute to both X-ray images below 20 keV and microwave images, they are produced from the plasma with different tempera-

tures and emission measures. The X-rays are mainly radiated from the plasma with higher temperature and lower emission measure, which was located at the top of the flare loops. While the microwaves are radiated from plasma with the lower temperature and larger emission measure (one order of magnitude larger than the emission measure obtained from RHESSI) plasma, which was located lower in the loops.

We found that the spectra of nonthermal electrons obtained from the OVSA microwave spectra are harder by 3.5-4.0 than those obtained from the RHESSI X-ray spectra. After eliminating the thermal contribution, the spectra of the nonthermal electrons obtained from NORH microwave fluxes at 17 and 34 GHz is still harder by 2.0 than that of the obtained from RHESSI. This difference of spectral slopes is within the range obtained by Silva, Wang, & Gary (2002) for their defined nonimpulsive flare category, and also agrees with the results from White et al. (2003), even the spectra of nonthermal electrons were obtained from RHESSI X-ray spectra above 100 keV.

Since the radio and HXR time profiles are so similar during the peak of the flare, we cannot argue that radio emission comes from a long-lived population of trapped electrons, while HXRS come from directly precipitating electrons (White et al. 2003). For the same reason, we also cannot agree that microwave-emitting electrons may be underwent a second stage acceleration. Therefore, in order to explain the different spectral slopes between X-ray and microwave emitting electrons, we may need to assume that two different electron populations are accelerated in different sites with distinct physical conditions, or even different acceleration mechanism.

We want to thank Brian Dennis for valuable discussion and critical comments on scripts, and Peter Gallagher for his help on SOHO data processing.

REFERENCES

- Aschwanden, M. J., Hudson, H. S., Kosugi, T., & Schwartz, R. A. 1996, *ApJ*, 464, 985
- Benka, S. G., & Holman, G. D. 1992, *ApJ*, 391, 854
- Brown, J. C., in Jr G. A. Newkirk (ed), *Coronal Disturbances*, IAU Symp. 57: 105
- Brown, J. C., & Emslie, A. G. 1987, *Sol. Phys.*, 110, 305
- Bruzek, A. 1964, *ApJ*, 140, 746

- Carmichael, H. 1964, In *The Physics of Solar Flares*, ed. W. N. Hess (NASA SP-50, Washington, DC:NASA), 451
- Ciaravella, A., Raymond, J. C., Li, J., Reiser, P., Gardner, L. D., Ko, Y.-K., & Fineschi, S. 2002, *ApJ*, 575, 1116
- Dennis, B. R. 1985, *Sol. Phys.*, 100, 465
- Dennis, B. R. 1988, *Sol. Phys.*, 118, 49
- Dennis, B. R., Veronig, A., Schwartz, R. A., Sui, L., Tolbert, A. K., Zarro, D. M., and the RHESSI Team 2003, *Adv. Space Res.*, Vol. 32, NO. 12, 2459
- Dulk, G. A. 1985, *ARA&A*, 23, 169
- Emslie, A. G., & Brown, J. C., 1980, *ApJ*, 237, 1015
- Emslie, A. G. 2003, *ApJ*, 595, L119
- Emslie, A. G. et al. 2004, *J. Geophys. Res.*, submitted
- Furth, H.P., Killeen, J., & Rosenbluth, M.N. 1963 Finite-resistivity instabilities of a sheet pinch, *Phys. Fluids*, 6, 459
- Gallagher, P.T., Dennis, B.R., Krucker, S., Schwartz, R.A., & Tolbert, A.K. 2002, *Sol. Phys.*, 210, 341
- Gan W. 2001, *ApJ*, 552, 858
- Gan, W. Q., Li, Y. P., Chang, J., McTiernan, James M., *Sol. Phys.*, 207, 137
- Garcia, H. 1994, *Sol. Phys.*, 154, 275
- Handy et al. 1999, *Sol. Phys.*, 187, 229
- Hirayama, T. 1974, *Sol. Phys.*, 34, 323
- Holman, G. D., & Benka, S. G. 1992, *ApJ*, 400, L79
- Holman, G. D. 2003, *ApJ*, 586, 606
- Holman, G. D., Sui, L., Schwartz, R. A., Emslie, A. G. 2003, *ApJ*, 595, L97
- Hudson, H. S. 1986, Characterization of Total Flare Energy, in *Energetic Phenomena on the Sun*, NASA Conf. Pub. 2439, Section 5.5, pp. 5-41- 5-47

- Hurford, G.J., et al. 2002, *Sol. Phys.*, 210, 61
- Kopp, R.A., & Pneuman, G.W. 1976, *Sol. Phys.*, 50, 85
- Ko, Y.-K., Raymond, J.C, Lin, J., Lawrence G., Li, J., Fludra, A. 2003, *ApJ*, 594, 1068
- Krucker, S., & Lin, R. P. 2002, *Sol. Phys.*, 210, 229
- Krucker, S., Hurford, G.J., Lin, R.P. 2003, *ApJ*, 595, 103
- Lin, R.P., Hudson, H. S. 1976, *Sol. Phys.*, 50, 153
- Lin, R.P., & Schwartz, R. A. 1987, *ApJ*, 312, 462
- Lin, R.P., et al. 2002, *Sol. Phys.*, 210, 3
- Lin, R.P., et al. 2003, *ApJ*, 595, L69
- Lin, J., & Forbes, T.G. 2000, *J. Geophys. Res.*, 105, 2375
- Lin, J. 2002, *Chinese J. Astron. Astrophys.*, 2, 539
- Masuda, S., Kosugi, T., Hara, H., Tsuneta, S., & Ogawara, Y. 1994, *Nature*, 371, 495
- Masuda, S., Kosugi, T., Hara, H., Sakao, T., Shibata, K., & Tsuneta, S. 1995, *Publ. Astron. Soc. Japan*, 47, 677
- Miller, J. A., Emslie, G. A., Holman, G. D., Cargill, P. J., Dennis, B. R., LaRosa, T. N., Winglee, R. M., Benka, S. G., & Tsuneta, S. 1997, *J. Geophys. Res.*, 102, 14631
- Nishio, M., Yaji, K., Kosugi, T., Nakajima, H., & Sakurai, T. 1997, *ApJ*, 489, 976
- Petrosian, V., Donaghy, T. Q., & McTiernan, J. M. 2002, *ApJ*, 569, 459
- Ramaty, R., Mandzhavidze, N., Kozlovsky, B., and Murphy, R. J. 1995, *ApJ*, 455, L193
- Silva, A. V. R., Wang, H., Gary, D. E. 2002, *ApJ*, 545, 1116
- Smith, D. M., et al. 2002, *Sol. Phys.*, 210, 33
- Smith, D. M., Share, G. H., Murphy, R. J., Schwartz, R. A., Shih, A. Y., & Lin, R. P. 2003, *ApJ*, 595, L81
- Sturrock, P.A., 1966, *Nature*, 211, 695

- Sui, L., Holman, G. D., Dennis, B. R., Krucker, S., Schwartz, R. A., & Tolbert, K. 2002, *Sol. Phys.*, 210, 245
- Sui, L., & Holman, G. D. 2003, *ApJ*, 596, L251
- Sui, L., Holman, G.D., Dennis, B.R. 2004, in press
- Švestka, Z., Fontenla, J.M., Machado, M.E., Martin, S.T., Neidig, D.F. and Poletto, G. 1987, *Sol. Phys.*, 169, 403
- Švestka, Z. 1996, *Sol. Phys.*, 108, 237
- Thomas, R. J., Crannell, C. J., and Starr, R. 1985, *Sol. Phys.*, 95, 323
- Tsuneta, S., Hara, H., Shimizu, T., Acton, L.W., Strong, K.T., Hudson, H.S., & Ogawara, Y. 1992, *PASJ*, 44, 63
- Veronig, A. M., Brown, J. C. 2004, *ApJ*, 603, L117
- Veronig, A. M., Brown, J. C., Dennis, B. R., Schwartz, R. A., Sui, L., & Tolbert, A. K. 2004, *ApJ*, submitted
- Webb, D. F., Burkepile, J., Forbes, T. G., & Riley P. 2003, *J. Geophys. Res.*, V108, Issue A12, pp. SSH 6-1
- White, S. M., Krucker, S., Shibasaki, K., Yokoyama, T., Shimojo, M., & Kundu, M. R. 2003, 595, L111
- Winglee, R. M. et al. 1991, *ApJ*, 375, 366

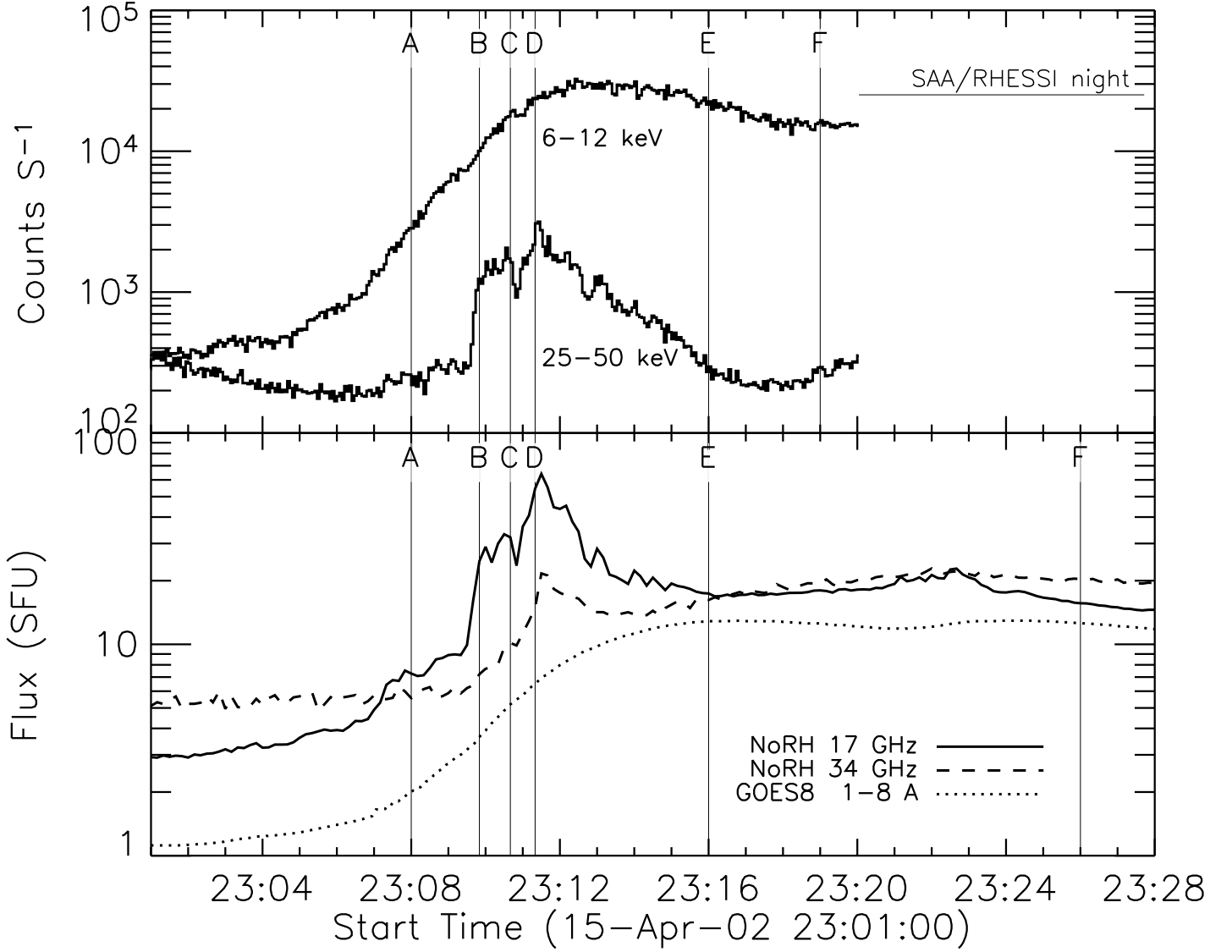


Fig. 1.— Light curves of the April 15 flare. The *upper panel* shows the RHESSI light curves in two energy bands (upper curve: 6–12 keV, lower curve: 25–50). The vertical lines indicate the start time of the each images in Fig. 13. The *lower panel* shows the time profiles of the NORH light curves in 17 GHz and 34 GHz. The GOES fluxes (1–8 Å) were adjusted to be shown in the same plot. The vertical lines indicate the start time of the each images in Fig. 11.

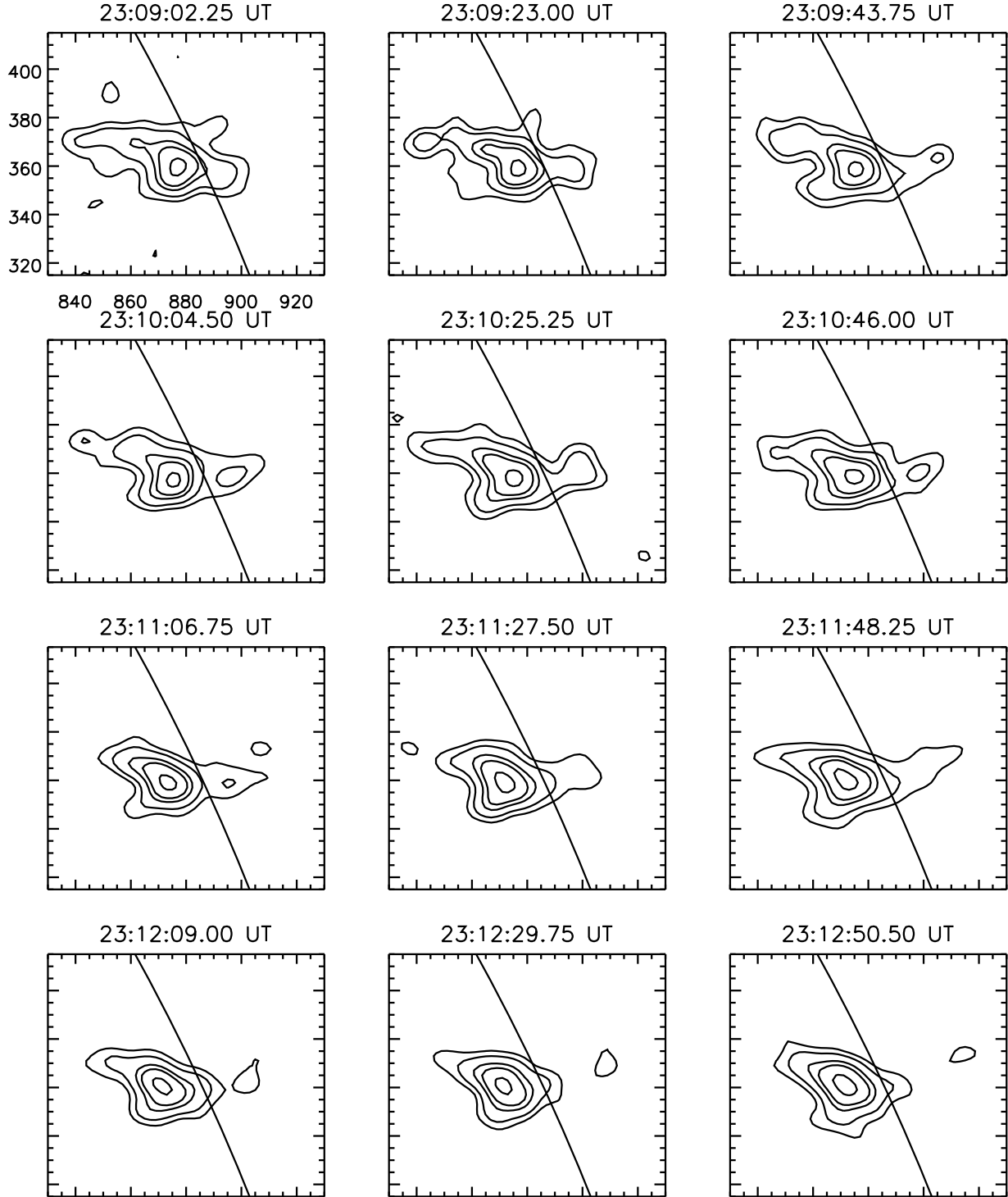


Fig. 2.— A time sequence of RHESSI 10-20 keV images for the 2002 April 15 flare. The images were reconstructed with CLEAN algorithm using grids 3-9, giving an angular resolution $\sim 7''$. The accumulation time of each images is 20 s. The start time of each image is indicated. The contour levels are 15, 25, 45, 60, and 90% of the peak flux in each image. The solid line denotes the solar limb.

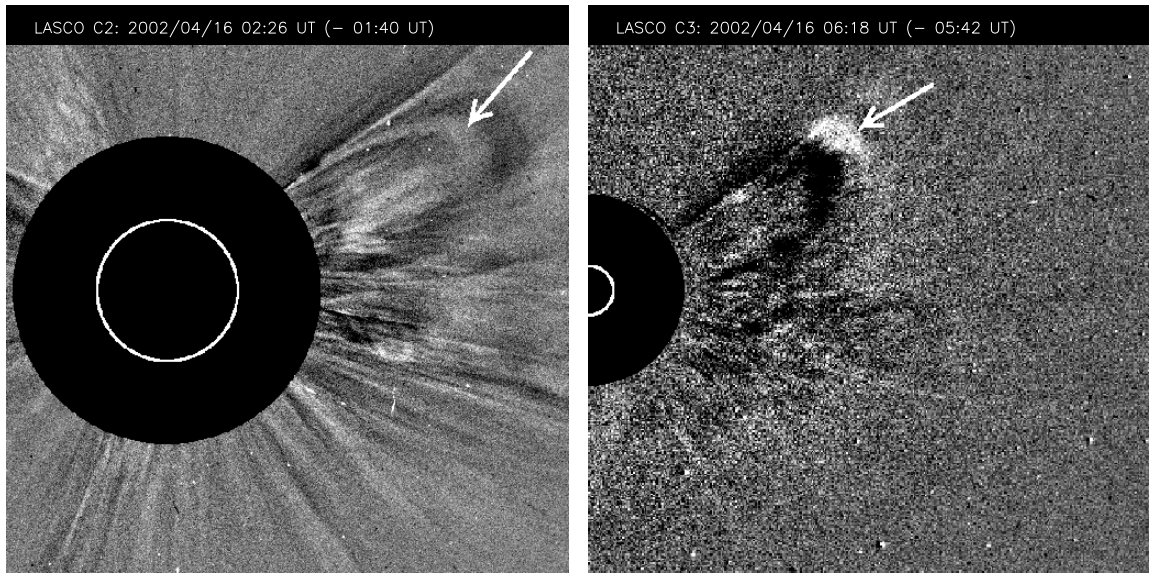


Fig. 3.— SOHO/LASCO C2 (left panel) and C3 (right panel) images on April 16, 2002. The arrow indicates the leading edge of the CME.

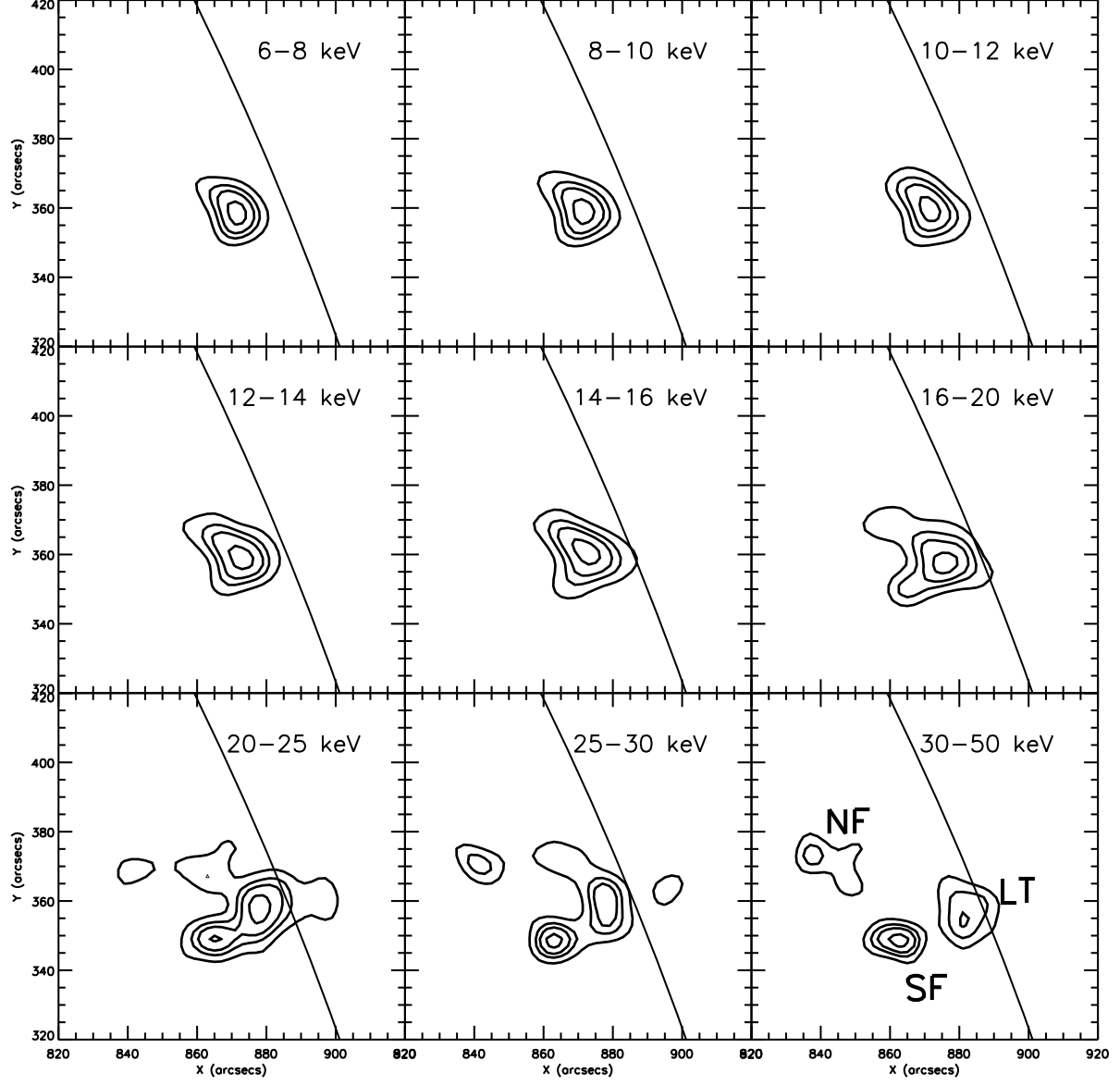


Fig. 4.— RHESSI images of different energy bands at the HXR peak (23:11-23:12 UT). The image reconstruction parameters are the same as in Fig. 2 except for the 1 min integration time.

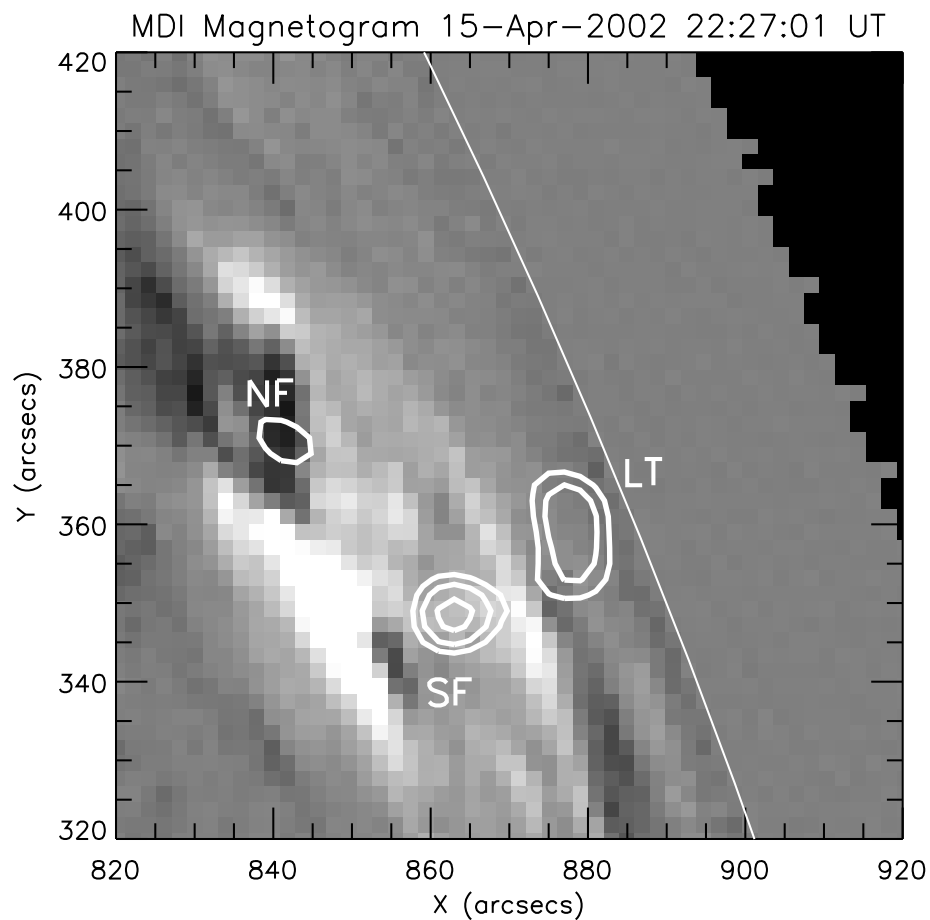


Fig. 5.— MDI magnetogram about 40 min before the flare started. The RHESSI 25-30 keV image at the major HXR peak was overlaid. The maximal magnetic field strength at the northern (‘NT’) and southern (‘ST’) footpoints are - 380 Gauss and + 280 Gauss, respectively.

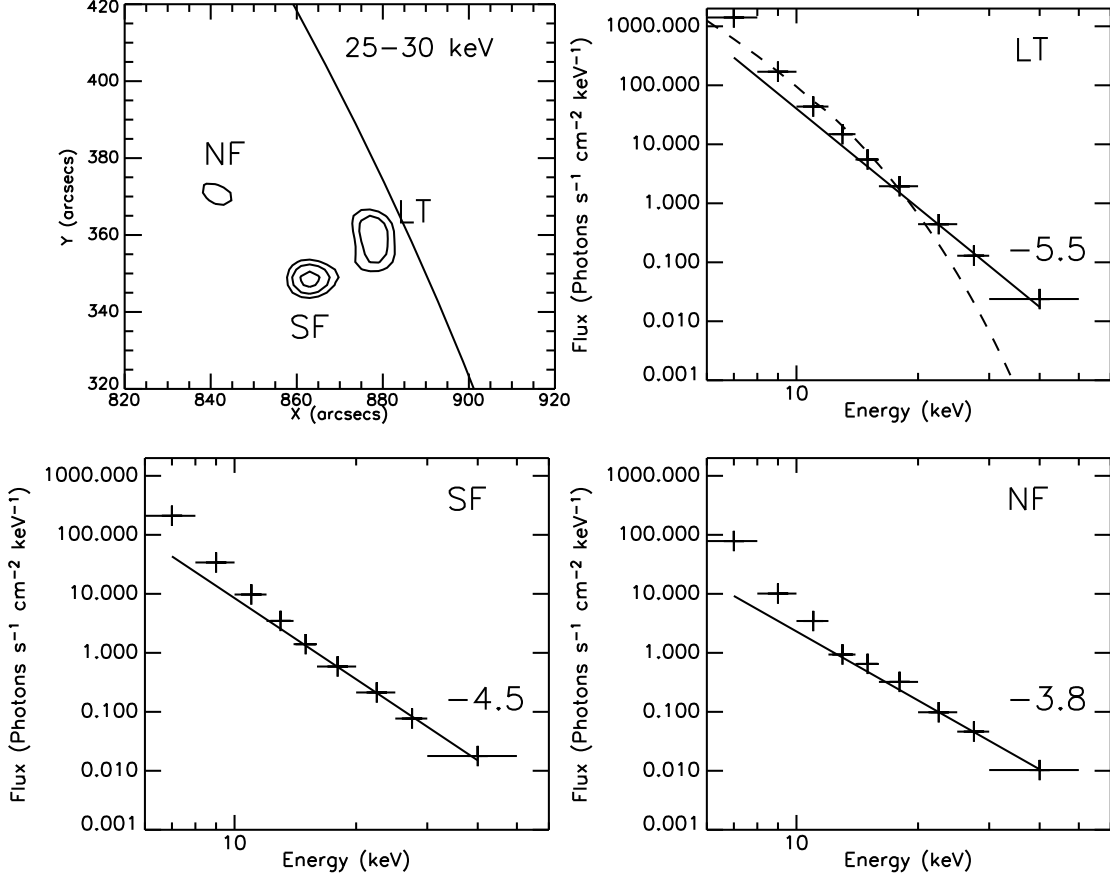


Fig. 6.— *Upper left panel* is the RHESSI 25-30 keV image (one of the images from Fig. 8), showing the three HXR sources: looptop source (or ‘LT’), southern footpoint (or ‘SF’), and northern footpoint (or ‘NF’). The contour levels are 55%, 70%, and 90% of the peak flux of the image. The accumulation time of the image is 60s (23:11-23:12 UT). The *upper right panel* shows the spectra of the looptop source. The dashed line shows the exponential component (using thermal bremsstrahlung model) of the spectra, fitted within the energy range between 10 keV and 20 keV. The emission measure and temperature of the plasma are $2 \times 10^{46} \text{cm}^{-3}$ and 30 MK, respectively. The solid line shows the power-law component (power-law index: -5.5) fitted within the energy range between 20 keV and 50 keV. The *lower two panels* shows the spectra of the southern and northern footpoints. The two spectra are only fitted with a power-law component at the energy range between 20 keV and 50 keV. The power-law indices are -4.5 and -3.8.

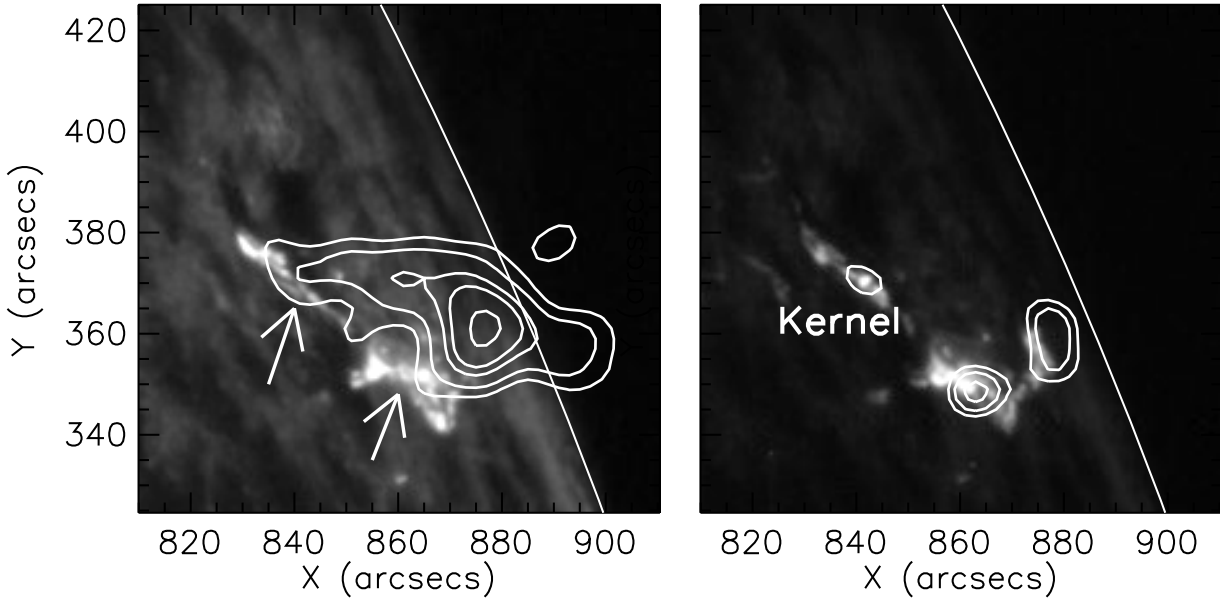


Fig. 7.— *Left Panel:* TRACE 1600 Å image at 23:09:01 UT (in the rise phase of the flare) overlaid with RHESSI 10-20 keV 23:09:02.25 UT. The arrows point to the two ribbons. *Right Panel:* TRACE 1600 Å image at 23:11:30 UT (at the major peak of the flare) overlaid with RHESSI 25-30 keV image at the peak.

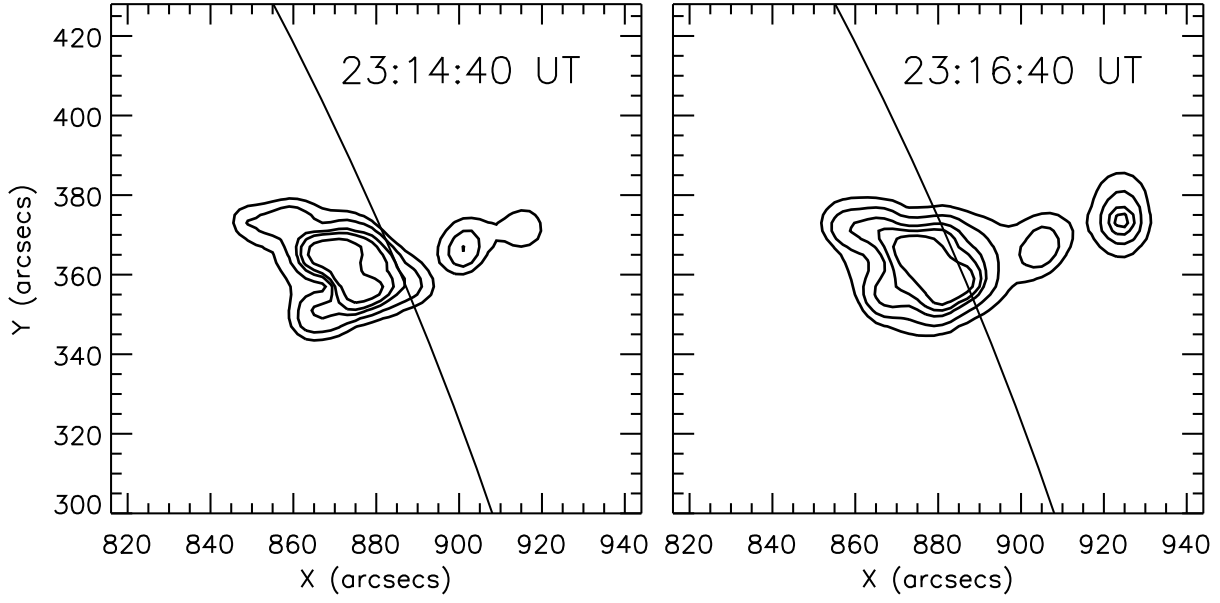


Fig. 8.— RHESSI 12-25 keV images at 23:14:40 UT (*left panel*) and 23:16:40 UT (*right panel*) showing coronal blobs believed to be evidence for magnetic islands produced by the tearing mode instability along a current sheet above the flare loop. The contour levels are 5, 10, 20, 30, and 50% of the peak flux of the images.

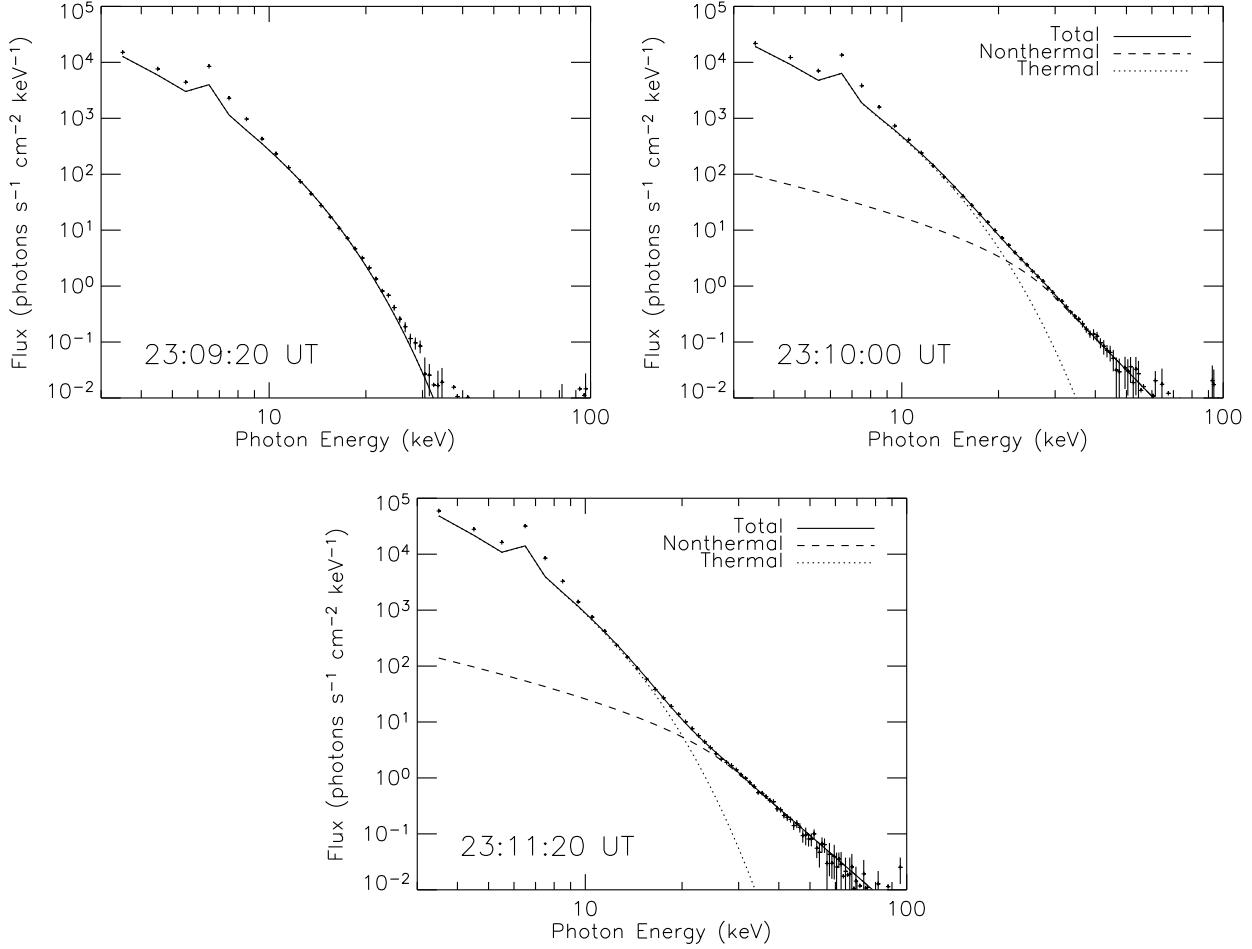


Fig. 9.— Three RHESSI spatially integrated spectra with background subtracted. *Upper left panel:* spectrum at the interval of 23:09:20-23:09:40 UT (right before the impulsive rise) fitted at the range of 10-20 keV. *Upper right panel:* spectrum at 23:10:00-23:10:20 UT (soon after the impulsive rise) fitted at the range of 10-50 keV. *Lower panel:* spectrum at 23:11:20-23:11:40 UT (at the major peak of the flare) fitted at the range of 10-50 keV. The plus signs with error bars represent spectral data. The lines represent model spectra: the dashed lines are from nonthermal thick-target bremsstrahlung; the dotted lines are from thermal bremsstrahlung; the solid lines are the summation of the two.

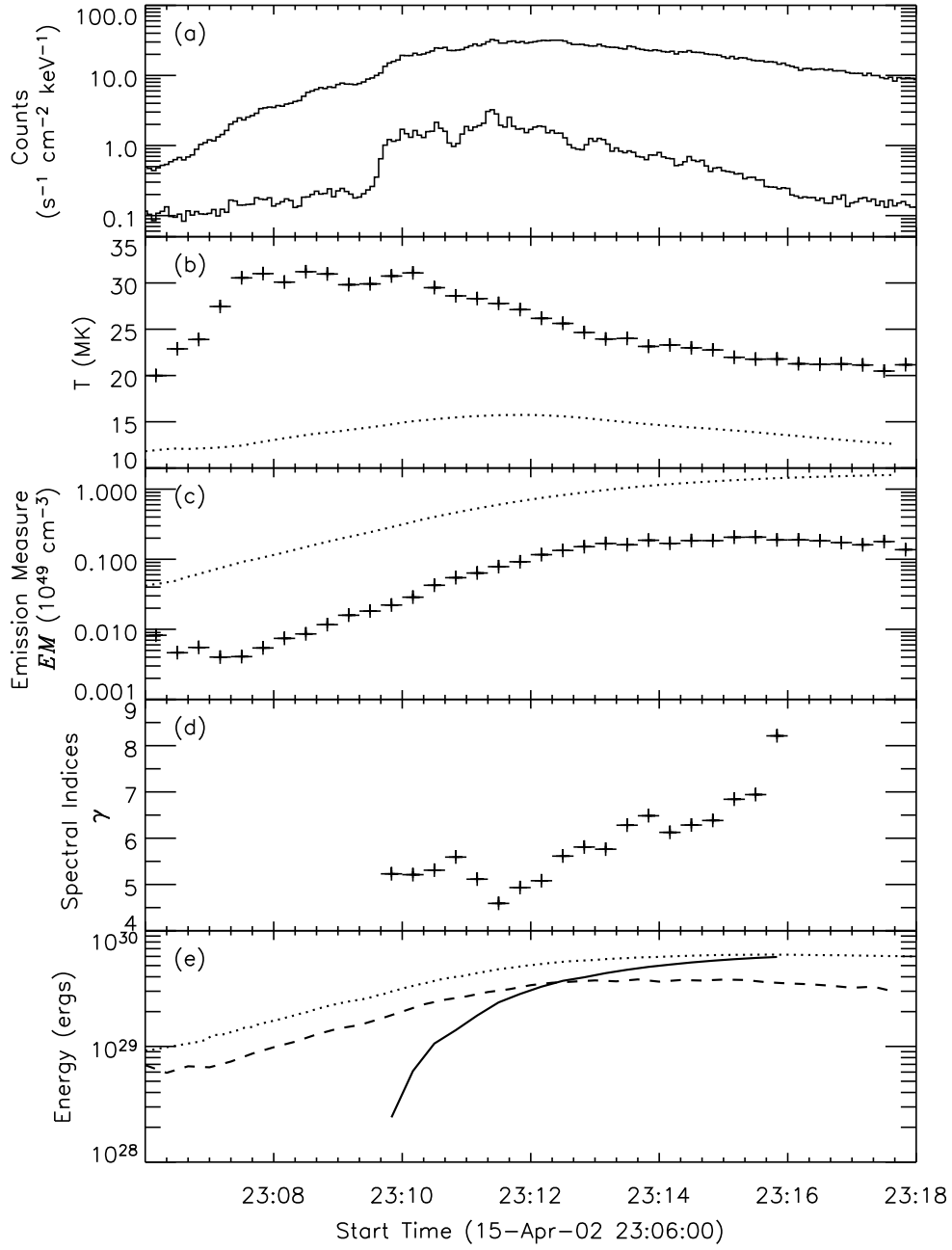


Fig. 10.— RHESSI spectral fitting results. *Panel a*: RHESSI light curves of 12-25 keV (*upper line*) and 25-50 keV (*lower line*). *Panel b*: plasma temperatures from RHESSI (*plus sign*) and GOES (*dotted line*). *Panel c*: plasma emission measures from RHESSI (*plus sign*) and GOES (*dotted line*). *Panel d*: power-law indices of photon spectra from RHESSI. *Panel e*: thermal plasma energy at each time interval from RHESSI (*dashed line*) and GOES (*dotted line*). The solid line represents the accumulated nonthermal electron energy.

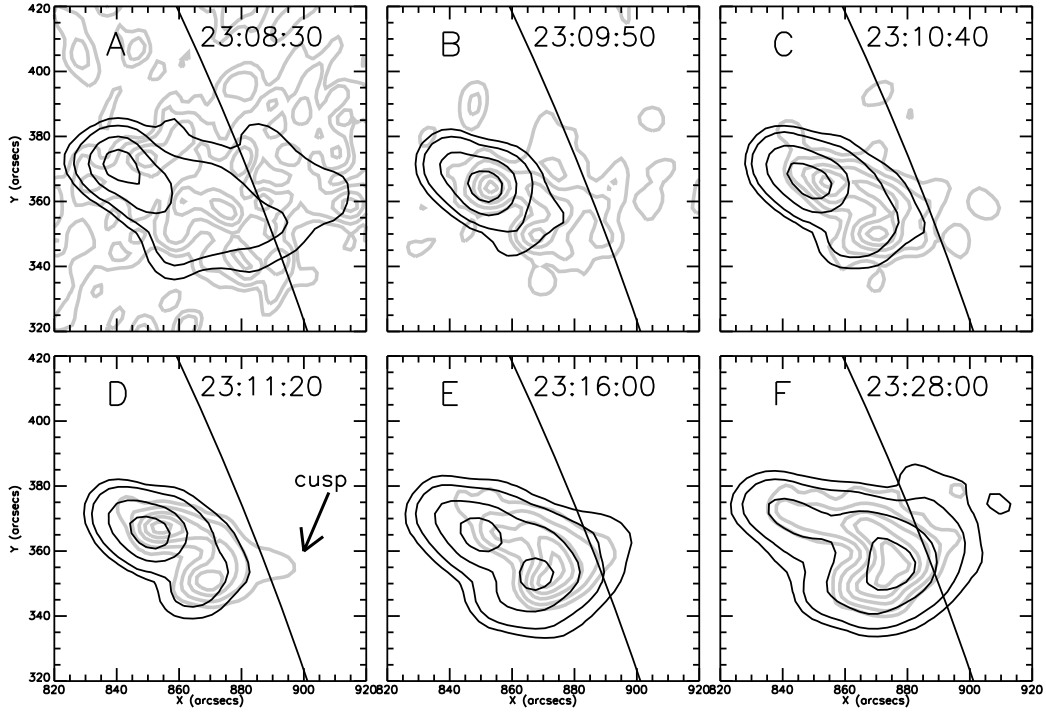


Fig. 11.— NORH microwave images at 17 GHz (*dark contours*) and 34 GHz (*light contours*). The contour levels are 5, 10, 30, and 70% of the peak flux in each image for 17 GHz, and 17, 30, 50, 70, and 90% for 34 GHz images. Based on the common features seen in both RHESSI and NORH, the NORH 17 and 34 GHz images were shifted within 5'' in both X and Y directions. The labels ('A'-'F') correspond to the labels in lower panel of Fig. 1.

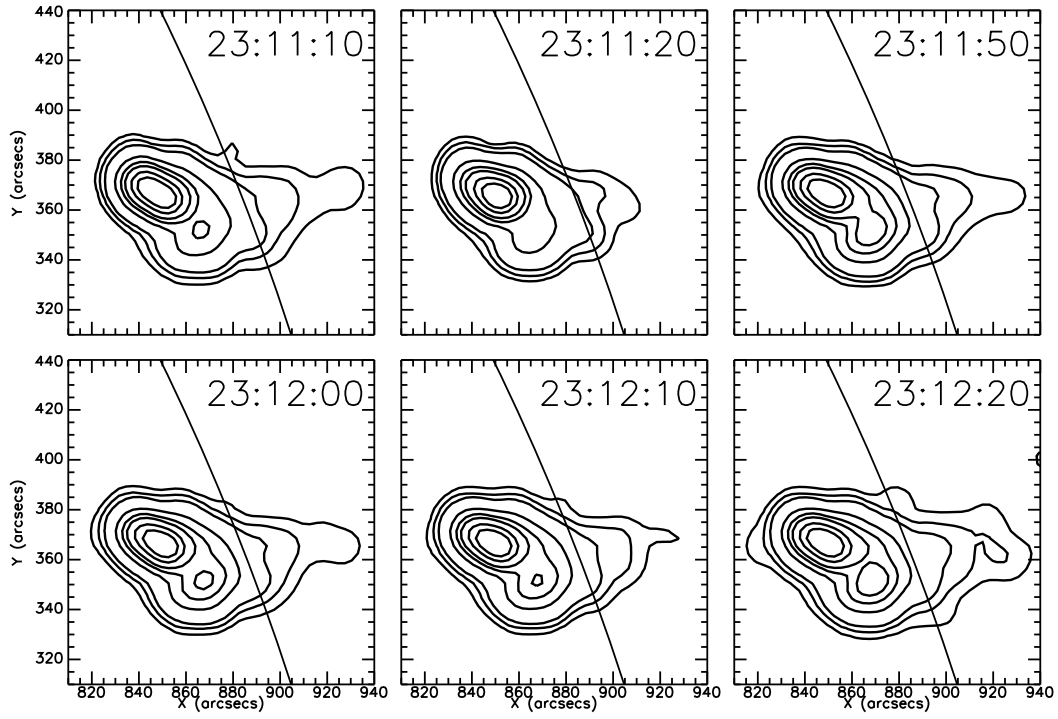


Fig. 12.— NORH 17 GHz images during the impulsive phase of the flare. The contour levels are 0.5, 1, 2, 10, 20, 30, 50, 70% of the peak flux in each image.

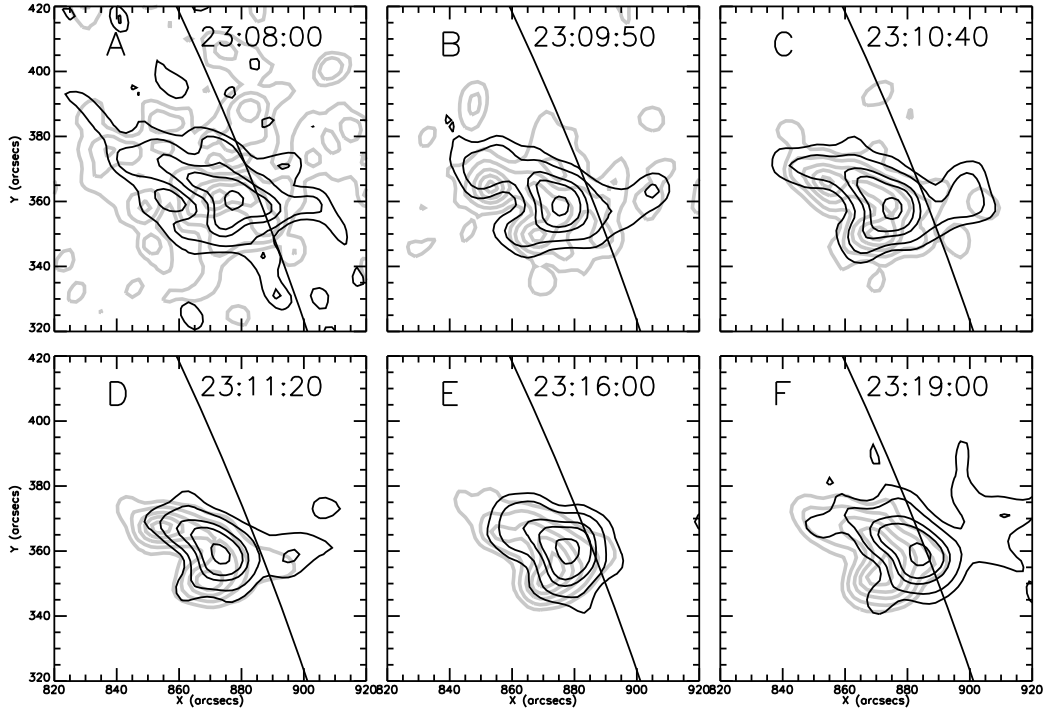


Fig. 13.— RHESSI 10-20 keV images (*dark contours*) and 34 GHz (*light contours*). The contour levels are 15, 25, 45, 60, and 90% of the peak flux in each image for RHESSI images. The 34 GHz images are the same as in Fig. 11. Based on the common features seen in both RHESSI and NORH, the 34 GHz images were shifted within 5'' in X and Y directions. The labels ('A'-'F') correspond to the labels in upper panel of Fig. 1.

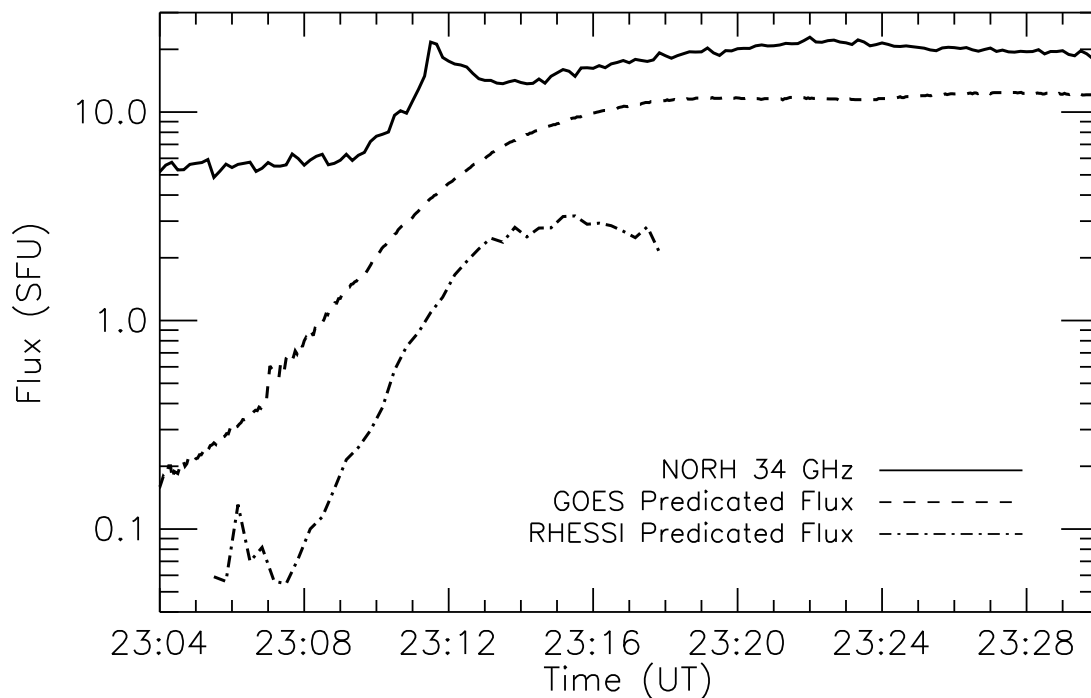


Fig. 14.— Comparison of NORH 34 GHz fluxes and calculated microwave fluxes (assuming free-free emission) from the thermal plasma observed by GOES and RHESSI.

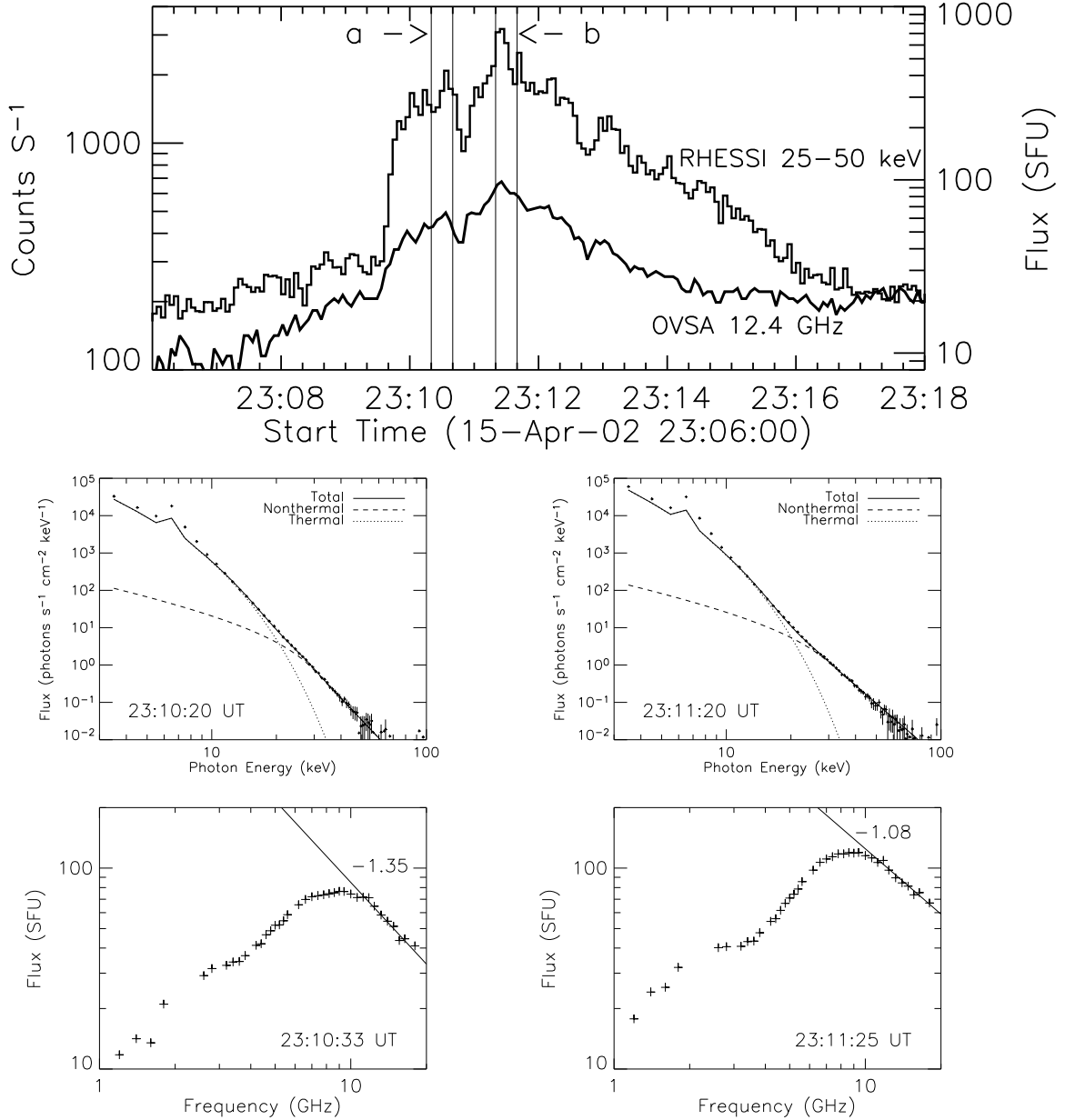


Fig. 15.— *Top panel:* Lightcurves of RHESSI 25–50 keV band and OVSA 12.4 GHz. The two intervals(a & b) for spectral fitting are indicated. *Middle row:* RHESSI spectra at the two intervals. The electron power-law indices are -6.8 and -6.0 for the left panel (interval a) and the right panel (interval b). *Bottom row:* OVSA spectra at the two intervals. The linear fits are made at the optically thin part of the spectra (from 12 to 18 GHz). The power law-indices are indicated.

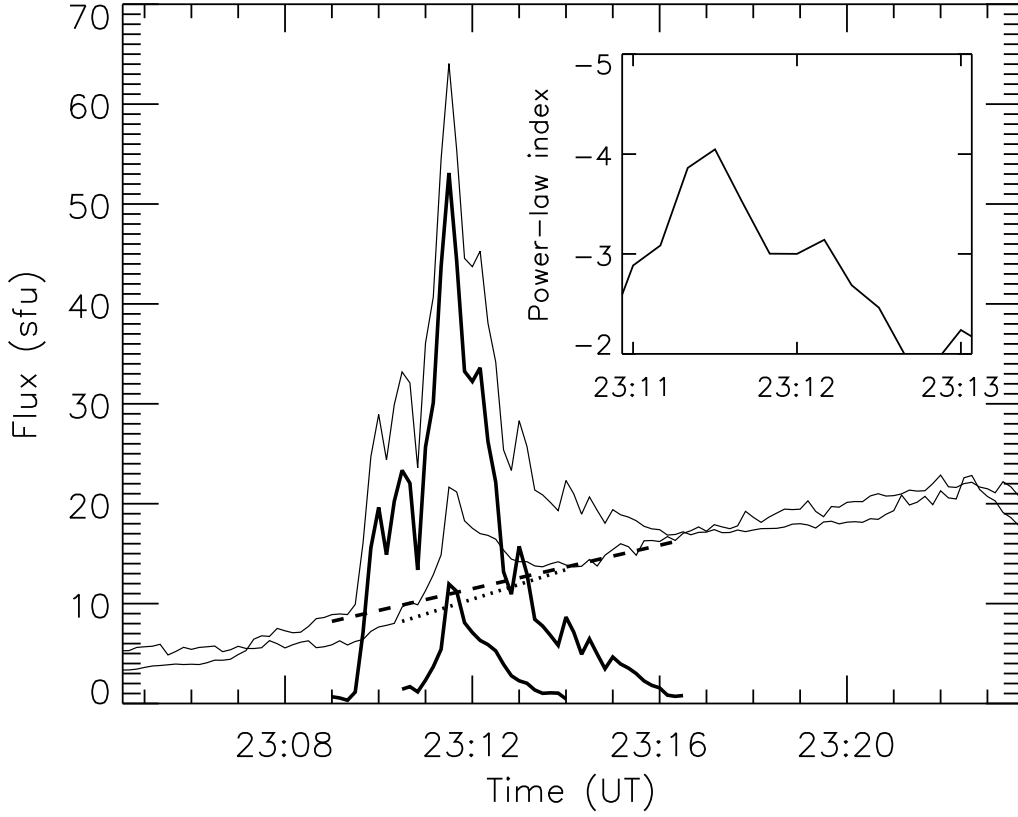


Fig. 16.— The *higher and lower thin solid line* represent the original NORH total fluxes at 17 and 34 GHz, respectively. The thermal fluxes of free-free emission at 17 (*dashed line*) and 34 GHz (*dotted line*) during the impulsive phase were obtained from linear extrapolation of the fluxes in the rise and decay phases. The deduced nonthermal gyrosynchrotron fluxes at 17 (*higher thick solid line*) and 34 GHz (*lower thick solid line*) were obtained by subtracting the thermal fluxes from the total fluxes at each frequency. The inset is the plot for the electron power-law indices at the impulsive phase obtained from the deduced nonthermal fluxes at two frequencies.